Politecnico di Milano

School of Industrial and Information Engineering

Master of Science in Space Engineering

POLITECNICO
MILANO 1863

Lyapunov Optimal Touchless Electrostatic Detumbling of Space Debris in GEO using a Surface Multisphere Model

Candidate
Fausto Casale
ID number 894084

Supervisor
Prof. James D. Biggs
Co-Supervisor
Prof. Hanspeter Schaub

Academic year 2018/2019

This thesis work has been made possible thanks to the collaboration between Politecnico di Milano and the Colorado University CU of Boulder, in particular the Autonomous Vehicle Laboratory (AVS) led by Prof. Hanspeter Schaub.

POLITECNICO
MILANO 1863

University of Colorado
Boulder

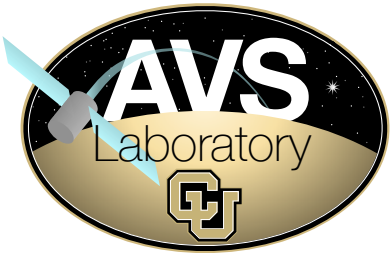

Fausto Casale: *Touchless Electrostatic Detumbling of Space Debris in GEO using a Surface Multisphere Model* | Master's thesis in Space Engineering, Politecnico di Milano, Milan, Italy.

Politecnico di Milano:
www.polimi.it

School of Industrial and Information Engineering:
www.ingindinf.polimi.it

Acknowledgments

I would like to give my thanks to Prof. Biggs and Prof. Schaub for believing in me during this international project and always being available to help me out when a doubt arose.

Thanks to my lab mates in Boulder, for accepting me into their family and being on my side during our shared semester of work.

Thanks to my family, my parents, my sister, aunts, uncles, cousins and grandparents, those that I can celebrate with and especially those who sadly can't anymore. You all gave me strength and support like the roots support a tree, without roots nothing can grow to reach the sky, thank you.

I also want to thank my friends in Bari, traveling companions in the path of our lives, with its up and downs we came all this way and we will walk together until the end, thank you Figli, thank you to my flatmates, thank you to everyone.

Thank you to my colleagues at Polimi, and all the friends I made in Milan, without you these last 6 years would have been 10 times as hard.

Thank you to my girlfriend Sabrina, for supporting me and never letting me feel guilty about chasing my dreams. I can't wait to see what the future holds for us.

And finally I also have to give my ironic "thanks" to the Covid-19 outbreak, this quarantine gave me the time to work on this thesis and gave me perspective on many aspects of life. I will not forget these frightening days but I can confidently say that I will not miss them when they are finally over.

Abstract

High tumbling rates of uncooperative targets pose strong technical challenges and collision risks that can prevent removal of the debris using contact strategies such as robotic arms or capture nets. Electrostatic touch-less de-tumbling is a promising technology that can be used to decrease an uncooperative object's rotational velocity in geosynchronous orbit (GEO), from a safe distance. This thesis demonstrates the advantages of applying a Lyapunov optimal control, in conjunction with a Surface Multi Sphere Model (SMSM) to describe the charge distribution. This approach allows for the analysis of general shapes, eliminating the need for analytical approximations on debris shape and expected torque, employed by previous work. Moreover, using this model, the robustness of the system to uncertainties to the debris center of mass position is tested. This analysis uncovers an unstable phenomena that was previously not captured using simpler models. An Active Disturbance Rejection Control (ADRC) ensures robustness of the system in the cases analyzed, also granting an increase in its effectiveness. It is shown in simulation that the system can exploit deviations in the center of mass to achieve a higher level of controllability and completely de-tumble all components of angular velocity.

Estratto

Le alte velocità di rotazione in detriti non cooperativi possono portare a significativi problemi tecnici e di sicurezza , che spesso rendono impossibile un'operazione di cattura con classici metodi di contatto, come bracci robotici o reti. Il detumbling elettrostatico è una nuova tecnica che consente di ridurre le rotazioni di un oggetto in orbita geostazionaria (GEO) senza necessitare di un contatto diretto. Questa tesi dimostra i vantaggi nell'utilizzare un legge di controllo Lyapunov optimal, applicata ad un Surface Multi Sphere Model (SMSM) che descrive la distribuzione di carica elettrica nei corpi. Questo approccio consente di modellare detriti dalla forma generica, eliminando le assunzioni fatte, in lavori precedenti, su forma del detrito e andamento analitico di forze e momenti torcenti imposti. Inoltre, usando questo modello, è possibile testare la robustezza del sistema a incertezze nella posizione del centro di massa e inerzia. Ciò ha portato alla scoperta di un comportamento instabile del sistema, che non poteva essere osservato con modelli più semplici, precedentemente utilizzati. Un Active Disturbance Rejection Control (ADRC) è implementato per garantire stabilità e robustezza alle incertezze considerate, migliorando anche la performance del processo stesso. Nei risultati è possibile osservare come il controllo migliorato può sfruttare le piccole deviazioni del centro di massa del detrito per ottenere una maggiore controllabilità del sistema e raggiungere un completo de-tumble di tutte le componenti di velocità angolare.

Contents

List of Figures

List of Tables

Software

The following software has been used for this thesis:

- 3D Builder – `https://www.microsoft.com/it-it/p/3d-builder/9wzdncrfj3t6?activetab=pivot:overviewtab`
- MATLAB v. R2019b and Simulink – `https://www.mathworks.com/products/matlab.html`
- Meshlab – `http://www.meshlab.net`

Nomenclature

$\mathcal{N}$	Inertial Frame centered in the service spacecraft
$\mathcal{B}$	Body Frame centered in the debris
$\boldsymbol{\omega}$	Angular velocity in body frame
$\dot{\boldsymbol{\omega}}$	Angular acceleration in body frame
$\boldsymbol{H}$	Angular momentum in body frame
$\boldsymbol{L}, \boldsymbol{L}^*$	Real and expected torque in body frame
T, T^*	Real and expected kinetic energy
$V(\boldsymbol{\omega})$	Lyapunov function
$\boldsymbol{Q}$	Charge vector containing the charge of each sphere
$\boldsymbol{\sigma}$	Charge density containing the charge density of each mesh triangle
$\boldsymbol{r}$	Position vector
$\boldsymbol{\epsilon}$	Error in torque estimation
$[J]^*$	Ideal diagonal Inertia matrix, its elements are $I_1,\ I_2,\ I_3$.
$\Delta[J]^*$	Inertia matrix uncertainty, randomly generated or manually set.
$[J]$	Real Inertia matrix, given by $[J]^* + \Delta[J]$
α	Radius scaling parameter for capacitance matching of SMSM
d	distance between the two objects centers of mass
β_1, β_2	Full state observer gains in the ADRC

Chapter 1

Introduction

1.1 Motivation

The accumulation of space debris in Earth orbit presents a significant risk to infrastructure and human presence in space [1, 2]. Active debris removal is one approach that has been proposed to mitigate this risk to existing space assets. This is especially challenging for debris in GEO, where the perturbations due to atmospheric drag and Earth oblateness are too small to ensure natural deorbiting, compared for example with low-Earth orbits (LEO), where the lifetime of a debris can be significantly shorter.
The total number of inactive objects in the geostationary belt has increased considerably over the last decade, leading to an accumulation of over a thousand of debris, several meters in size, far surpassing the number of total active spacecraft in orbit (around 500) [3–5]. The value of space assets, essential for communication, in the region of GEO is estimated to be 13 Billion US dollars[6], so protecting these objects from potentially catastrophic impacts is a priority.
Moreover, debris removal in this region is important not only to protect existing satellites from impact, but also because each of these objects occupies a portion of space very valuable, that could be used by another operational satellite. Indeed the available spots in GEO will inevitably become scarcer with time, if nothing is done to prevent that.

1.2 State of the art

Most concepts for de-orbiting an uncooperative object, involve the use of a chaser spacecraft that brings itself close to the debris and de-tumbles and de-orbits it by imposing forces and torques mechanically on the debris. [7–11]. This requires the service spacecraft to touch the object, posing significant risks since this can be tumbling uncontrollably with rates up to 10 deg/s [12, 13].

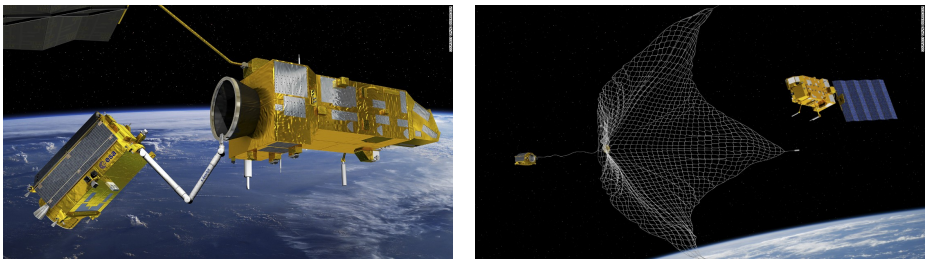

(a) Robotic arm (b) Capture net

Figure 1.1: Two contact de-tumble strategies, images taken from cnn.com

This value surpasses the current requirements of de-orbiting technology, that is estimated to be around 1 deg/s [8–11]. It is then necessary to reduce these rotations before employing the de-orbit technology. This can be done using different contact strategies, reference [14] lists quite a few.
All of them require the service craft to attach to the debris, this can be done in three main ways: with an harpoon, with a net or with a perch.

The harpoon is an object launched at the debris, that connects to it by piercing the body in a certain soft point, while still attached to the service craft with a link. This concept requires knowledge of the debris structure to correctly select an appropriate location to aim for, and the ability to time the release correctly. If the incorrect portion of the debris is hit, the harpoon may bounce off, knock pieces off or it may even trigger an explosion. Moreover even if the attachment is successful, as the end of the cable wraps around the tumbling debris, it will likely pulling the service craft towards the debris at high speed. The system would have to be designed to account for this.

A net would be a similar concept that does not require any specific attachment point to be aimed for, but the net itself has to be designed to be able to deploy correctly and wrap around several possible debris shapes. Once it is positioned, there is still the same problem in which the service has to "reel in" the debris, that could prove very difficult if the debris is spinning at a fast rate.

Lastly, a perch consists in a stiff arm with microspines at the extremities that dig in the debris much like a climber ice pick digs in a wall. The location of the attachment point is not predetermined in this case, since it all depends on what surface asperities the perch hooks on and this is difficult to predict and control. The rigid arms give more control on the effect of the debris on the service, provided that the link is able to handle the resulting loads.

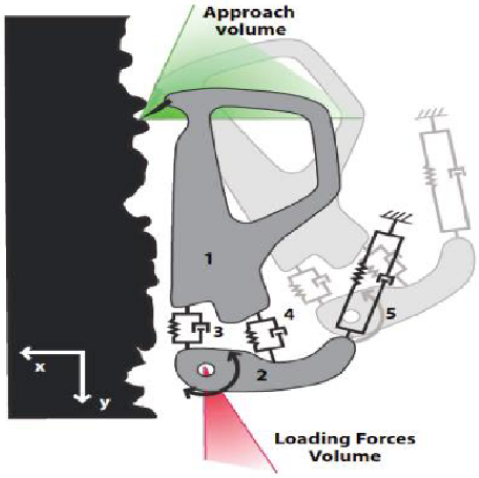

Figure 1.2: Perch attachment, figure taken from [14]

Once the service is correctly attached and tumbling with the debris two main effects can be employed to de-tumble the system: impose a torque that dissipates the angular velocity, or increase the angular Inertia so that the rotations decrease thanks to the conservation of angular momentum.

Applying a dissipating torque can be done in numerous ways, like for example using magnetic torquers, either inflatable or fixed; using the rope deployed to attach the debris to act as a winch once it is wrapped around it; also a swarm of nano sats can be used, each with a propulsive system capable of providing enough thrust to generate the desired torque or even directly de-orbit the debris.

Increasing the angular inertia of the debris with attachable masses or expanding foam, will decrease its rotational velocity but does not ensure a full de-tumble and also grants very little controllability. The evolution of the rotations will only depend on the dynamics of the system itself. It is also possible to cut the debris in smaller pieces and separate them with ropes, in order to increase the inertia even further.

A more in depth analysis is given in [14], but in the end it can be said that despite everything, most of the problems that these solutions have to face have the same origin: the need of a contact between debris and service spacecraft.

It would be preferable to perform the de-tumble at a safe distance from the debris itself, so that the issues listed above can be avoided. For this reason different touchless de-tumbling strategies have been developed, like the Ion-beam Shepard[15, 16] or Electrostatic de-tumbling[17–19].

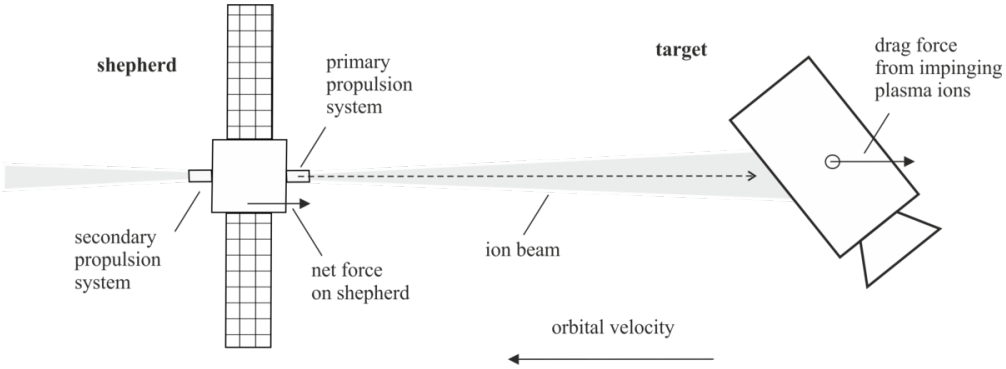

Figure 1.3: Diagram of Ion Shepherd basic principle

Both of these methods trade the speed and effectiveness of a contact strategy for the reduced risk of impacts and ability to handle high tumbling rates.

In the case of the Ion Shepard, an ion beam is used to shoot heavy ionized particles on the debris surface. The forces generated by this impact on the debris can be used to create torques that de-tumble the debris or also be directly used to remove it from orbit in a matter of 3 to 4 months, so that no contact is required at all.
One drawback of this method could be the burst of particles that are generated by the ablation of the material hit by the Ion beam. These plumes could hit delicate components of the debris or (more importantly) of the service craft and could thus damage them, also the momentum given by these ejection of material could modify the behaviour of the de-tumble. Great care must be taken in trying to anticipate this behaviour and possibly use it to boost performances. Despite these minor problems the Ion Shepherd still represents a valid alternative for touchless de-tumbling and it is being currently researched.

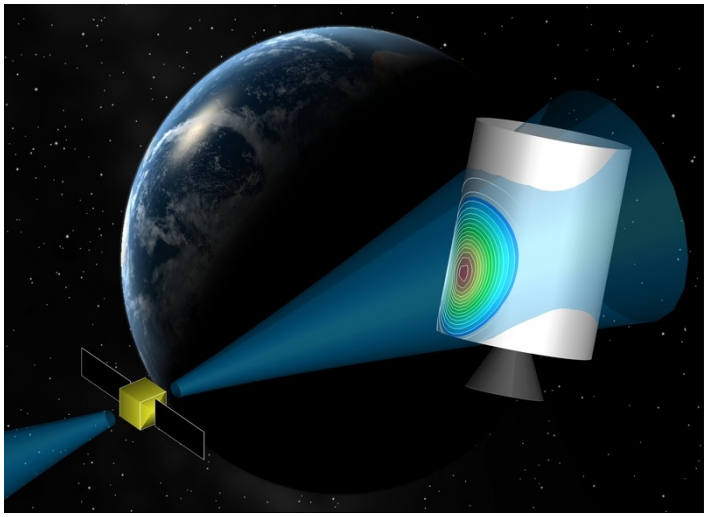

Figure 1.4: Ion-Beam Shepard, taken from leonsweep.com

1.3 Thesis Objectives

The electrostatic de-tumbling is the touchless de-tumble alternative examined in this thesis. Electrostatic charging is used to directly generate forces and torques on the debris by taking advantage of the Coulomb law. In recent years, studies have been conducted on the feasibility of imposing an electric potential on a debris and a service spacecraft, using electron beams and ion emitters [20]. Then using the electrostatic forces generated, the rotational kinetic energy of the debris can be decreased touchlessly and even a net push or pull force can be applied to de-orbit the object. [21, 22].

Reference [20] shows that this is feasible to accomplish using current technology, moreover it is possible to charge objects to tens of kilovolts in a matter of microseconds and using as little as watts level electric power. In GEO the charged objects are able to exert significant electrostatic forces even with separation distances of tens of meters, because Debeye lengths are approximately around 200 m [23, 24]. This is not possible in high density plasma environments, such as in LEO, where the effects of Debeye shielding are much more intense[25].

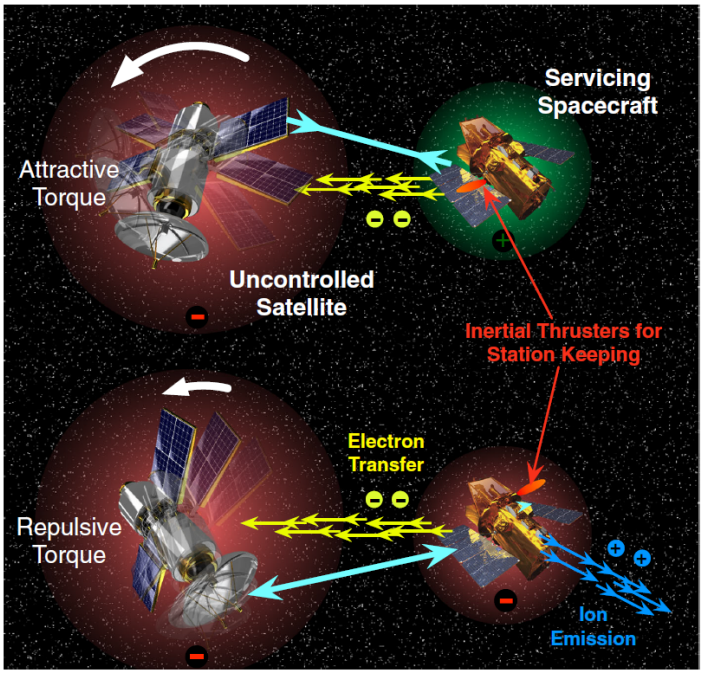

Figure 1.5: Electrostatic detumbling, taken from [26]

In order to predict the generated torques and thus compute the voltage required at faster than real time, the Multi Sphere Model (MSM) has been developed [27]. It models the charge distribution as a population of spheres placed in various parts of the body. Based on the radius of the spheres and their position, the MSM computes the charge contained in each sphere by solving a linear system and then the forces and torques can be obtained in a fraction of a second. A more in depth theoretical background is given in chapter 2.

In previous work [21, 22, 26], the MSM has been applied to study the detumbling of an axial-symmetric cylindrical debris, where the torque around the transversal axes could be modeled as a function of the angle ϕ between the symmetry axis and the service craft position. This way the torque and thus the potential to impose can be directly obtained from analytical functions $L(\phi)$ and $V(\phi)$, this allows to make some considerations on equilibrium conditions of the system and their stability, but some generality is lost in the process. No effect on the rotations around the symmetry axis is considered, and also the results obtained do not apply to general shapes.

This thesis implements the method developed in [28] to generate a MSM of complex shapes and simulate the de-tumbling by computing the generated forces and torques by directly applying the Coulomb law on each sphere, instead of relying on analytical functions. The control strategy employed is a Lyapunov optimal controller that aims to obtain the fastest decrease of kinetic energy possible, by selecting the correct voltage to impose at each time step. This new

control law is also able to handle general spacecraft tug and debris geometries, since it does not rely on any shape assumption.

Once the detumbling has been performed for an ideal case, the robustness of the system to various types of uncertainties is analyzed, the control system is then improved based on the results obtained. For example, the application of an Active Disturbance Rejection Control (ADRC) [29–32], that estimates the lumped uncertainties accounting for them in the control, is tested.

Chapter 2

Multi Sphere Model

In order to correctly control the system, a certain degree of knowledge of the charge distribution is required. There are different ways to compute the electric charge in an object, going from the simplest point charge assumption to a Finite Element Model, each with its different advantages and drawbacks. Simple models like point charge and effective sphere are quick to setup and can give acceptable results for applications like formation flying or in general when only the net force effect on the body is necessary. If, like in the case of this study, a more in depth knowledge of the distribution across the body is required, a more precise model is necessary, with the best one being a Finite Element Model. A FEM analysis can not be performed at faster than real time though and requires several minutes if not hours to complete.

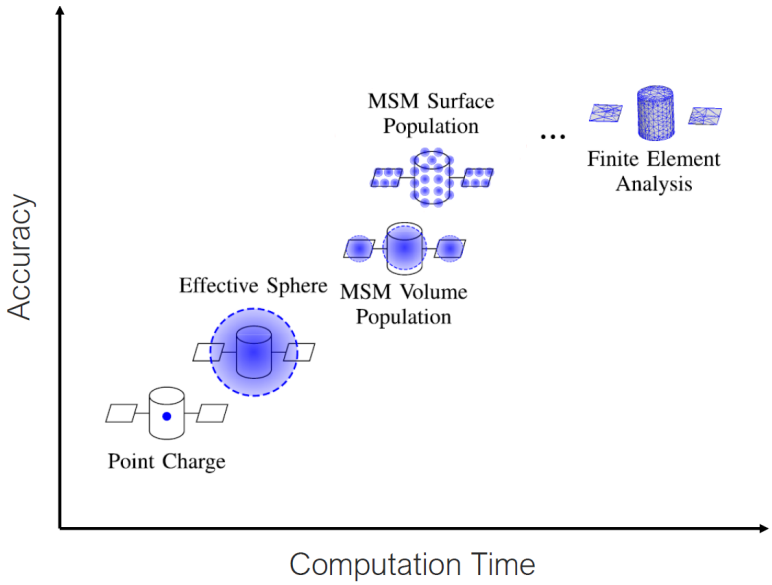

Figure 2.1: Comparison of different methods of computing electric charge distribution, picture taken from [33]

The Multi Sphere Model is a middle ground between these two extremes, that can be used to estimate charge distribution generated in a body with a given potential at faster than real time speed. In general the object is approximated with a group of spheres that, based on their size, distance from one another, and imposed electric potential, contain a certain amount of charge. The electrostatic forces can then be computed by applying the Coulomb's law on each sphere pair. The model assumes the bodies to consist of uniform conductors, which is reasonable for most spacecrafts due to the high conductivity of the external Mylar protective layers [34]. The higher the number of spheres, the more precise the results obtained are going to be, but also the computational effort will rise, so different techniques have been developed to choose the correct model for the case considered. In this chapter the two different versions of the MSM will be presented: the Volume Multi Sphere Model (VMSM) and Surface Multi Sphere Model (SMSM).

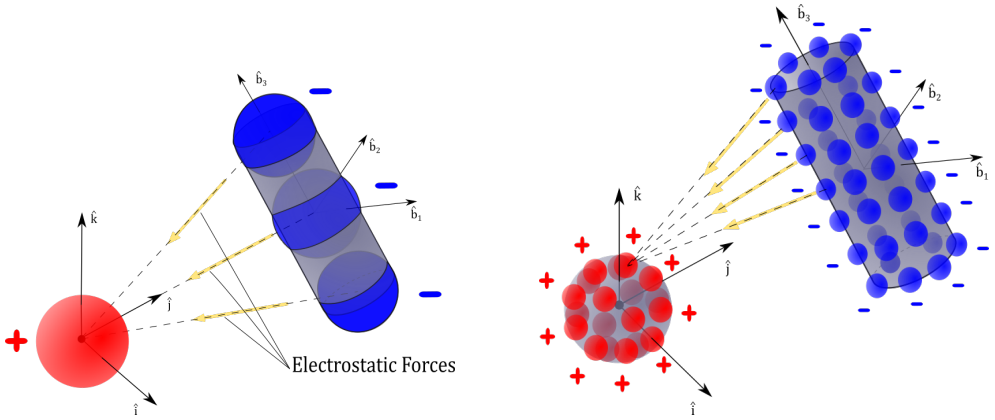

(a) VMSM (b) SMSM

Figure 2.2: Same geometry represented using the two Multi Sphere Models

Both of these models represent the body as N spheres with variable position and radii, they only differ in the number, size and placement of the spheres in the conductor. The voltage on any sphere is a function of both its own charge and the charge of all nearby spheres. If these spheres are far enough away to be approximated as point charges, the voltage is given by:

$$V_i = \frac{1}{4\pi\epsilon_0}\frac{q_i}{R_i} + \sum_{j=1,j\neq i}^{n} \frac{1}{4\pi\epsilon_0}\frac{q_j}{r_{i,j}} \tag{2.1}$$

q_i and R_i are respectively the charge and radius of the i^{th} sphere, $r_{i,j}$ is the distance between the i^{th} and j^{th} spheres and ϵ_0 is the permittivity of free space constant.

For a total of N spheres this can be summed up in the linear system:

$$\begin{bmatrix} V_1 \\ V_2 \\ \vdots \\ V_N \end{bmatrix} = \frac{1}{4\pi\epsilon_0} \begin{bmatrix} 1/R_1 & 1/r_{1,2} & \cdots & 1/r_{1,N} \\ 1/r_{2,1} & 1/R_2 & \cdots & 1/r_{2,N} \\ \vdots & \vdots & \ddots & \vdots \\ 1/r_{N,1} & 1/r_{N,2} & \cdots & 1/R_N \end{bmatrix} \begin{bmatrix} Q_1 \\ Q_2 \\ \vdots \\ Q_N \end{bmatrix} \tag{2.2}$$

$$\boldsymbol{V} = [S]\boldsymbol{Q} \qquad \boldsymbol{Q} = [C]\boldsymbol{V}$$

Note how the elastance matrix $[S]$ and its inverse $[C]$ only depend on the geometry of the body and its spheres, so they do not change if the shape of the body stays constant. The procedure to select position and radius of the spheres depends on the model used.

2.1 Volume Multi Sphere Model

The Volume MSM (VMSM) represents the body as a small number of relatively big spheres, positioned in its volume, each of these spheres has a specific radius and position that are varied by an optimizer to best match force and torque data produced by a commercial FEM program[26]. This is repeated for several relative position and attitudes, until a set of parameters can be identified, that best describe the system in all possible different conditions.

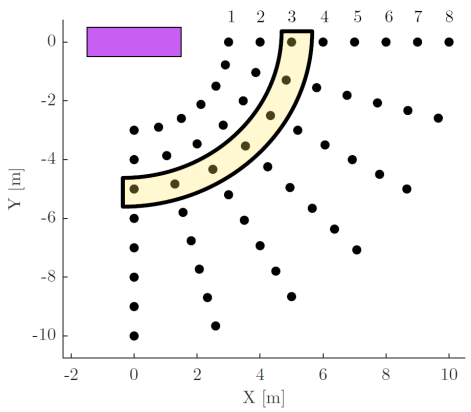

Figure 2.3: Example of position sweep performed in [35]

This procedure is slow, since a FEM model must be generated for each of these points and this could require hours of hand tuning and computations. Following studies have found that matching the electric field generated by the electric charge is easier since only one body needs to be modeled [35, 36] but still it requires several hours of work. This method has been used in cases of simple shapes like the one depicted in Fig.2.2 where no torque around the symmetry

axis was considered. Also it works very well when the separation distance between the two objects is above 10 craft radii, but its precision decays quickly as the distance decreases.
As stated before, control laws that use this model assume a certain expected analytical torque function, that depends on the inclination of the cylinder axis, completely ignoring any possible effect on the angular velocities around the symmetry axis[17–19]. In fact it is easy to see that the model depicted in Fig.2.2a can not describe any symmetry axis torque, since the spheres are perfectly aligned along it. It is also possible to generate more precise models, by increasing the number of spheres distributed in the object's volume, thus granting a better description of the torque in all axes but again the position in which the spheres are generated can be arbitrary and complex to implement.

2.2 Surface Multi Sphere Model

The second model switches to generating a greater number of spheres on the conductor surface and is thus called Surface MSM (SMSM) [33]. It is faster to setup and it yields more precise torque estimations with just a small increase of computational effort. Also it represents more accurately the behavior of real electric charges, that always position themselves on the objects' surface.
The spheres were initially positioned homogeneously on the surface but this does not give enough flexibility for general shapes and is also hard to setup in the case of curved surfaces. It has been found that using a triangular mesh to divide the object surface leads to better results[28, 33], it also simplifies the process itself since these meshes can be easily generated for most shapes. The radii of the spheres are selected by matching the diagonal elements of the elastance matrix $[S]$ from Eq. 2.2 to the ones given by a different theoretical model, that could be for example the boundary element method or the method of images[28].
In this thesis the method described in [28] is employed, it uses the Method of Moments to provide a foundation for convergence of the results. The spheres are positioned in the centroids of the mesh triangles and the radii are obtained from the MOM elastance matrix elements:

$$R_i = \frac{1}{4\pi\epsilon_0 S_{i,i}} \tag{2.3}$$

The procedure to obtain $S_{i,i}$ is described in Chapter 3.
The main advantages given by the SMSM are the greatly reduced setup times, since the truth model used for its matching are much faster to compute than performing a FEM analysis multiple times.
Also the SMSM gives better results for separation distances within 10 craft radii. This is because by having an higher number of spheres, the system has more degrees of freedom to redistribute its charge and induced effects can be considered.

For example, let's observe the situation depicted in this figure:

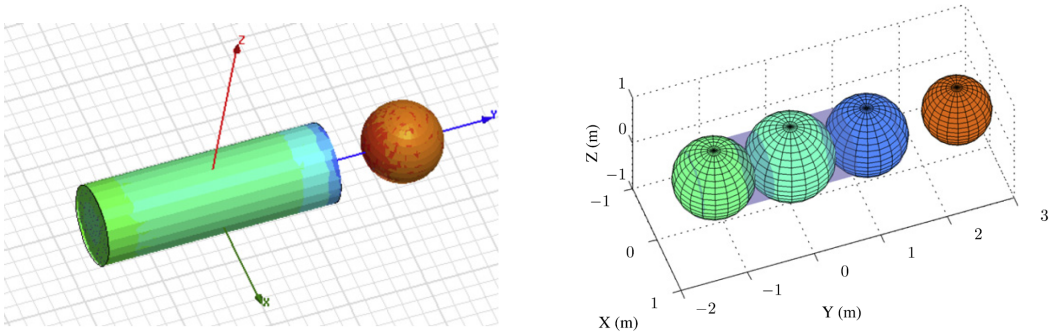

(a) FEM (b) VMSM

Figure 2.4: Surface charge comparison between FEM and VMSM, figure taken from [27]

As it can be seen, representing the system with only 4 total spheres greatly limits the distribution in charge that is present in the real case. The spherical spacecraft can only be described as an equipotential sphere and only three distinct charge levels are present in the cylinder. In the case of a SMSM the real case is represented more accurately at the cost of an increased computational burden. This may be worth it when the two objects are at close distance, where these induced effects are more intense, but it is a waste of resources when the two objects are at more than 10 craft radii of separation.
Another benefit is that since the number of spheres considered only depends on the number of triangles in the mesh, it is easier to control the precision of the model and the same geometry can be easily modeled with different levels of accuracy. The analysis performed takes advantage of this by employing different models of varying precision, to observe how the performances of the de-tumble are affected.
Moreover most of the procedure can be completely automatized, apart from the generation of the 3D model itself, so there is no time consuming manual tuning required.

From all the alternatives, the SMSM generated from the Method of Moments has been picked because it combines both high precision of the charge description and simplicity of use for general geometries. In the next chapter the generation of the model itself is explained more in detail.

Chapter 3

Model Generation Procedure

In this chapter the SMSM is generated for the two objects considered: the service spacecraft and the debris. First a triangular surface mesh is created, then the Method of Moments (MOM) is applied to the mesh to generate the sphere distribution. Finally the capacitance of the isolated body is computed and matched to a thruth model, in order to improve performances. Once the model of the two objects are obtained they are put together to build up the system itself.

3.1 Mesh generation

A triangular mesh that describes the object external surface as a series of triangles is generated, the higher the number of triangles used, the more precise the model, with a higher number of spheres generated and thus a higher computational complexity to the simulation. These meshes can be created manually, generating each vertex and edge, but this is only feasible when using very simple shapes like cubes and cylinders. It is far easier to use a 3D modeling software to create stl files manually or starting from already existing 3D CAD models.

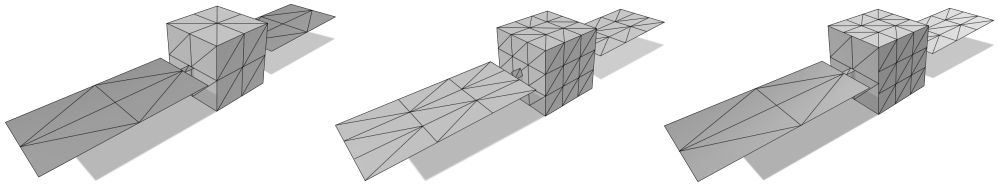

(a) 68 faces (b) 160 faces (c) 127 faces mix

Figure 3.1: Three different levels of mesh precision

The software used during this study is 3D Builder [37], usually used for 3D printing, so each part of the system can be customized to have as many triangles

as necessary. By changing only a few parameters, it is possible to create .stl files of many different number of total triangles for the same shape, even with a heterogeneous distribution, for example by concentrating most spheres on the parts closer to the debris (Fig.3.1c). The meshes are also modified using MeshLab [38] in order to refine some aspects and delete triangles that may not be necessary.
This is especially important in situations where two surfaces are close together and can be described as a single plane, like in the case of solar panels. If not addressed, this could lead to spheres that are too close together, creating numerical singularity issues when the elastance matrix $[S]$ and its inverse, the capacitance matrix $[C]$, are computed. The reason for this is explained at the end of the next section.

3.2 From MOM to SMSM for the isolated object

Once the mesh is created, the MOM is used to compute the charge distribution on each of the N triangles the surface is divided into. This method is based on the Gauss theorem, applied on each triangle (for a more in depth description see [28]):

$$V(\boldsymbol{r}) = \int \frac{\mathrm{d}q'}{4\pi\epsilon_0 ||\boldsymbol{r} - \boldsymbol{r}'||} \tag{3.1}$$

Where $\boldsymbol{r}$ is the observation point considered and $\boldsymbol{r}'$ is the source point. If the source region is discretized into area elements A_i, the voltage is:

$$V(\boldsymbol{r}) = \frac{1}{4\pi\epsilon_0} \left(\int_{A_1} \frac{\mathrm{d}A'}{||\boldsymbol{r} - \boldsymbol{r}'||} \sigma_1 + \int_{A_2} \frac{\mathrm{d}A'}{||\boldsymbol{r} - \boldsymbol{r}'||} \sigma_2 + \cdots \right) \tag{3.2}$$

Where σ_i is the surface charge density on the i^{th} area element.
For all the triangles the following linear system is built:

$$\begin{bmatrix} V_1 \\ V_2 \\ \vdots \\ V_N \end{bmatrix} = \frac{1}{4\pi\epsilon_0} \begin{bmatrix} \int_{A_1} \frac{\mathrm{d}A}{||\boldsymbol{r}_1 - \boldsymbol{r}'||} & \int_{A_2} \frac{\mathrm{d}A}{||\boldsymbol{r}_1 - \boldsymbol{r}'||} & \cdots & \int_{A_N} \frac{\mathrm{d}A}{||\boldsymbol{r}_1 - \boldsymbol{r}'||} \\ \int_{A_1} \frac{\mathrm{d}A}{||\boldsymbol{r}_2 - \boldsymbol{r}'||} & \int_{A_2} \frac{\mathrm{d}A}{||\boldsymbol{r}_2 - \boldsymbol{r}'||} & \cdots & \int_{A_N} \frac{\mathrm{d}A}{||\boldsymbol{r}_2 - \boldsymbol{r}'||} \\ \vdots & \vdots & \ddots & \vdots \\ \int_{A_1} \frac{\mathrm{d}A}{||\boldsymbol{r}_N - \boldsymbol{r}'||} & \int_{A_2} \frac{\mathrm{d}A}{||\boldsymbol{r}_N - \boldsymbol{r}'||} & \cdots & \int_{A_N} \frac{\mathrm{d}A}{||\boldsymbol{r}_N - \boldsymbol{r}'||} \end{bmatrix} \begin{bmatrix} \sigma_1 \\ \sigma_2 \\ \vdots \\ \sigma_N \end{bmatrix} \tag{3.3}$$

Then each element in the central matrix is divided by the area of the element to change the units of the elements to farad^{-1} and change the vector on the right from the charge density $\boldsymbol{\sigma}$ to the total charge $\boldsymbol{Q}$.

$$\boldsymbol{V} = [S]\boldsymbol{Q} \qquad \boldsymbol{Q} = [C]\boldsymbol{V} \tag{3.4}$$

In this study the potential is assumed equal for all elements $V_1 = V_2 = V_N = V_{\text{body}}$, then in order to compute the resulting charge, the Elastance matrix $[S]$ is inverted to obtain the Capacitance matrix $[C]$.
Since the triangular elements are chosen as basis area, the elements of $[S]$ can be rewritten by considering two generic triangles (i and j) both formed by the corners $[\boldsymbol{ABC}]$ as shown in the next figure:

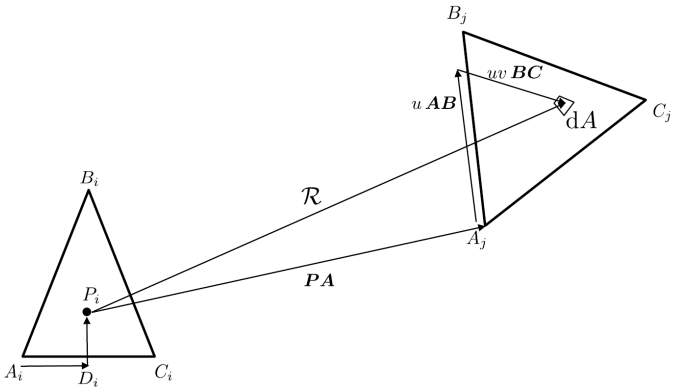

Figure 3.2: triangular coordinate system taken from [28]

The separation term $\mathcal{R} = ||\boldsymbol{r}_N - r'||$ can be written as $||\boldsymbol{PA} + u\boldsymbol{AB} + uv\boldsymbol{BC}||$ where u and v are the parameterized coordinates, and the the area differential becomes $\mathrm{d}A = u||\boldsymbol{AB} \times \boldsymbol{BC}||\mathrm{d}u\mathrm{d}v$.
This leads to the elements of $[S]$ being computed as:

$$S_{i,j} = \frac{1}{4\pi\epsilon_0 A_j} \int_0^1 \int_0^1 \frac{u||\boldsymbol{AB} \times \boldsymbol{BC}||\mathrm{d}u\mathrm{d}v}{||\boldsymbol{PA} + u\boldsymbol{AB} + uv\boldsymbol{BC}||} \tag{3.5}$$

The integrals are solved numerically using the adaptative quadratic algorithm. This procedure, while giving accurate results, is computationally heavy, since it requires one to solve N^2 integrals at each sampling time. Therefore, this is only done once to setup the parameters for the SMSM by matching the elements of $[S]$.

This is possible because the SMSM relates potential and charge in the system in a similar way, with the following linear system:

$$\begin{bmatrix} V_1 \\ V_2 \\ \vdots \\ V_N \end{bmatrix} = \frac{1}{4\pi\epsilon_0} \begin{bmatrix} 1/R_1 & 1/r_{1,2} & \cdots & 1/r_{1,N} \\ 1/r_{2,1} & 1/R_2 & \cdots & 1/r_{2,N} \\ \vdots & \vdots & \ddots & \vdots \\ 1/r_{N,1} & 1/r_{N,2} & \cdots & 1/R_N \end{bmatrix} \begin{bmatrix} Q_1 \\ Q_2 \\ \vdots \\ Q_N \end{bmatrix} \tag{3.6}$$

As it can be seen the charge on each i^{th} sphere depends only on its radius R_i and the distance from all the other spheres $r_{i,j}$, so the matrix $[S]$ stays constant as long as the object doesn't change its shape.
The radius of the sphere is obtained by inverting the diagonal elements of the $[S]$ matrix given by the MOM in Eq.3.3, the spheres are then positioned at the centroid of each triangle. This leads to good matching of all the elements of the two $[S]$ matrices, if the mesh has an high enough amount of triangles, otherwise the errors increase noticeably. This happens because the resulting matrix is mostly diagonal unless the radii of the spheres are too big compared to the spheres distance (spheres should not intersect) leading to singularity effects when computing the inverse.
The elements of this matrix only depend on the geometric properties of the isolated body and are conserved during rigid body rotations or translations, so they can be computed only once during the pre-processing phase, as demonstrated in [34, 39].
Because of this property the $[S]$ matrix referred to the single body is called the self-elastance matrix.

3.3 Capacitance matching and two body setup

The total capacitance of the isolated body is computed by summing all the elements of the self-capacitance matrix $[C]$. This can be used to obtain an estimate of the capacitance of complex shapes, if a high sphere count model is considered. Scaling the computed radius of the spheres to obtain the same total capacitance of a truth model (FEM model or high number SMSM) increases the precision of the computed torques and forces without increasing the computational effort [28].

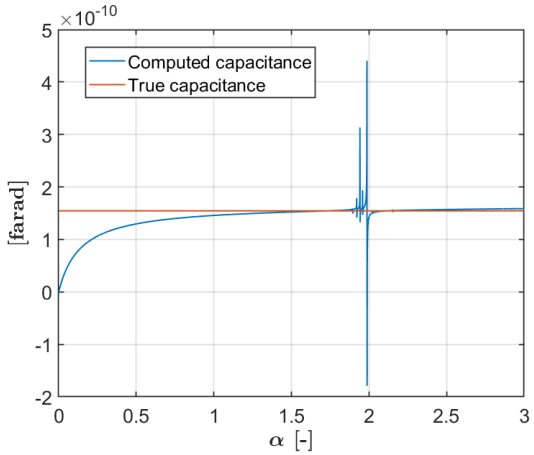

Figure 3.3: How capacitance changes by scaling the radiuses of the SMSM of a parameter α

So the radiuses of the SMSM obtained are scaled by a radius parameter α, until the total capacitance matches the desired value or at least comes as close as possible without leading to any numerical instabilities (depicted in Fig.3.3). This can generate considerable errors in the estimated charge distribution.
Once this has been done for both bodies considered (service craft and debris), the two can be put together to compute the interactions between the charged elements. In particular the charge will redistribute based on the distance between each sphere that is changing with the debris tumbling motion.
The obtained linear system can be summed up to obtain:

$$\begin{bmatrix} \boldsymbol{V}_1 \\ \boldsymbol{V}_2 \end{bmatrix} = \begin{bmatrix} [S_1] & [Sm] \\ [Sm]^T & [S_2] \end{bmatrix} \begin{bmatrix} \boldsymbol{Q}_1 \\ \boldsymbol{Q}_2 \end{bmatrix} \tag{3.7}$$

Where $[S_1]$ $(N \times N)$ and $[S_2]$ $(M \times M)$ are the constant self-elastance square matrix of the service and debris respectively, and the elements of $[Sm]$ are made up by the inverse of the distance between the spheres of the two different bodies and these are the elements that change during the tumbling motion.

Also $\boldsymbol{V}_1$ and $\boldsymbol{V}_2$ represent vectors with the imposed potential for each sphere of the two bodies, same for charge vectors $\boldsymbol{Q}_1$ and $\boldsymbol{Q}_2$.

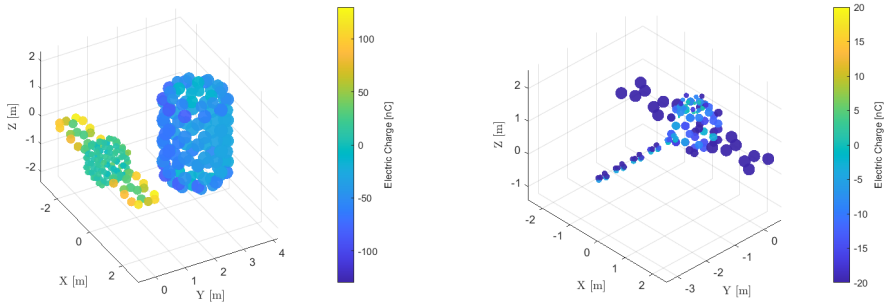

(a) Box and panel servicecraft and cylindrical debris

(b) Box and panel servicecraft with antenna and magnetometer boom

Figure 3.4: Examples of SMSM

Given this particular structure of the total elastance matrix the Schur complement method can be used to obtain the capacitance matrix without having to recompute the full matrix at each time step.

$$\begin{pmatrix} A & B \\ C & D \end{pmatrix}^{-1} = \begin{pmatrix} (A - BD^{-1}C)^{-1} & -(A - BD^{-1}C)^{-1}BD^{-1} \\ -D^{-1}C(A - BD^{-1}C)^{-1} & (D - CA^{-1}B)^{-1}) \end{pmatrix} \tag{3.8}$$

Once the charge distribution is obtained, the forces and resulting torques for each sphere pair (N spheres on service craft and M spheres on debris) are computed using Coulombs law and the total torques acting on the bodies are obtained.

$$\boldsymbol{F}_j = \sum_{i=1}^{N} \frac{1}{4\pi\epsilon_0} \frac{Q_i Q_j}{{r_{ij}}^3} \boldsymbol{r}_{ij} \tag{3.9}$$

$$\boldsymbol{L} = \sum_{j=1}^{M} \boldsymbol{r}_{j|b} \times \boldsymbol{F}_j \tag{3.10}$$

First the total force $\boldsymbol{F}_j$ on each j sphere of the debris is computed by summing all Coulomb contributions from each i sphere of the service. Then the total torque $\boldsymbol{L}$ acting on the debris is obtained by summing up all the contributions given by the cross product between the position of the j sphere in body coordinates $\boldsymbol{r}_{j|b}$ and the total force resulting on it $\boldsymbol{F}_j$.

Once the model of the system is ready, the behavior of the electric charges can be computed in a fraction of a second. Given a certain electric potential on the two objects, the total resulting torque on the debris is obtained, so now a way to correctly choose what potential to give the debris and the service craft is necessary. This control law needs to pick the potential based on data that is available from the sensors of the service only, these are values like angular velocity and attitude of the debris with all the errors and uncertainties that this includes.
In the next chapter the dynamical system used to simulate the de-tumbling is presented and the Lyapunov optimal control law employed is described.

Chapter 4

System Description

The dynamical system uses two different frames of reference, depicted in Fig.2.2: a fixed one called $\mathcal{N}$ $(\boldsymbol{i}, \boldsymbol{j}, \boldsymbol{k})$ that is centered in the service spacecraft center of mass and a body frame $\mathcal{B}(\boldsymbol{b}_1, \boldsymbol{b}_2, \boldsymbol{b}_3)$ centered at the debris center of mass that is initially set at a certain distance d on the axis $\boldsymbol{j}$.
Only rotations of the debris are considered, this is because the service spacecraft is assumed to use thrusters to offset the resulting torques on it. This assumption can be considered reasonable given the low intensity of the resulting torques (around 10^{-7} Nm for the symmetry axis and 10^{-4} Nm for the others) also the same thrusters are assumed to be able to keep the separation distance imposed, as demonstrated in [22].

4.1 System description

At each time step, the relative attitude between the two frames is described by the Direction Cosine Matrix (DCM) $A_{B/N}$ and used to compute the resulting electrostatic torques on the debris using the SMSM and equations 3.9 and 3.10. In particular the torques are first computed by the controller, that selects the electric potential to impose on the objects based on a less precise sphere population (Fig.3.1a), then this potential is given to the physics model that computes the real value of the resulting torques, using a better sphere model (Fig.3.1b), that are then applied to the system.

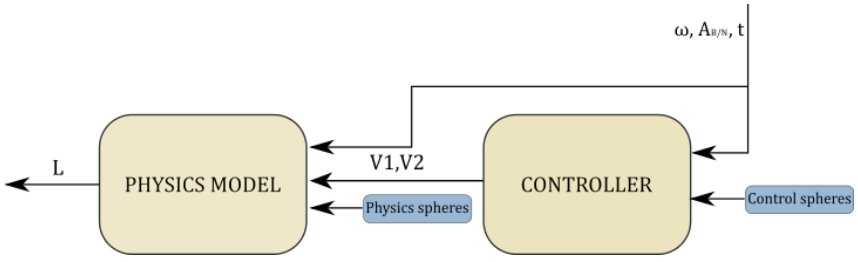

Figure 4.1: Controller and physics simulation structure

Thanks to the customization proprieties of the SMSM it is thus possible to mimic the modeling errors that are present in a real case and study their effect on the system performance. Ideally the physics population would have a spheres count in the thousands, to better represent the real charge distribution but this is limited by the performances of the machine used to run the simulation.
Also no uncertainties in angular velocity reading or attitude imprecision are included, it is assumed that the service spacecraft is able to reconstruct the debris state using cameras or LIDAR with an error well below 0.1 deg/s for velocity and 10 cm for the position of the debris. This would not contribute significantly to the performance of the de-tumble and is a reasonable assumption given the precision granted by modern imaging systems [40–42].
Beside the parts depicted in Fig.4.1 the system is composed by the blocks that compute the angular velocity (Euler's equations), the one that computes the DCM and errors in torque estimations.
After the electrostatic torque is computed, more effects can be added like Solar Radiation Pressure torques, gravity gradient and center of mass deviations, this way it is possible to study the effects these aspects have on the debris and the de-tumbling performance.

4.2 Control law

The Lyapunov optimal control law used to ensure the de-tumbling of the debris is based on the minimization of the Lyapunov function V($\boldsymbol{\omega}$) [43], defined as the expected total kinetic energy of the debris. From now on all estimated quantities are identified with an asterisk:

$$V(\boldsymbol{\omega}) = T^* = \frac{1}{2}\boldsymbol{\omega}^T[J]\ \boldsymbol{\omega} \tag{4.1}$$

$$\dot{V}(\boldsymbol{\omega}) = \dot{T}^* = \boldsymbol{\omega}^T[J]\ \dot{\boldsymbol{\omega}} = \boldsymbol{\omega}^T([J]\boldsymbol{\omega} \times \boldsymbol{\omega} + \boldsymbol{L}^*) = \boldsymbol{\omega}^T\boldsymbol{L}^* \tag{4.2}$$

The angular velocity $\boldsymbol{\omega}$, the expected torque $\boldsymbol{L}^*$ and inertia matrix [J] are expressed along the principal axes in body coordinates, also the term $[J]\boldsymbol{\omega} \times \boldsymbol{\omega}$ is deleted since it is perpendicular to $\boldsymbol{\omega}$ and thus its scalar product goes to zero.
The expected torque $\boldsymbol{L}^*$, that is different from the real one evaluated in the physics model, depends on the imposed potential on the two objects, so the Lyapunov derivative also depends on the chosen potential V_1 for the spacecraft and V_2 for the debris.
Initially the controller was given the ability to pick both potentials from an interval of $\pm$20 kV but first results showed that $\dot{T}^*$ varies almost linearly with the imposed potential as it can be seen in Fig.4.2, and also that the value does not change if the two potentials V_1 and V_2 are swapped. Since the objective of the de-tumbling is to decrease the kinetic energy as fast as possible without a

real interest in the final attitude of the debris, only the maximum values of ±20 kV are evaluated for the service spacecraft and the debris is kept at a constant 20 kV, effectively limiting the controller to a Bang-Bang control.

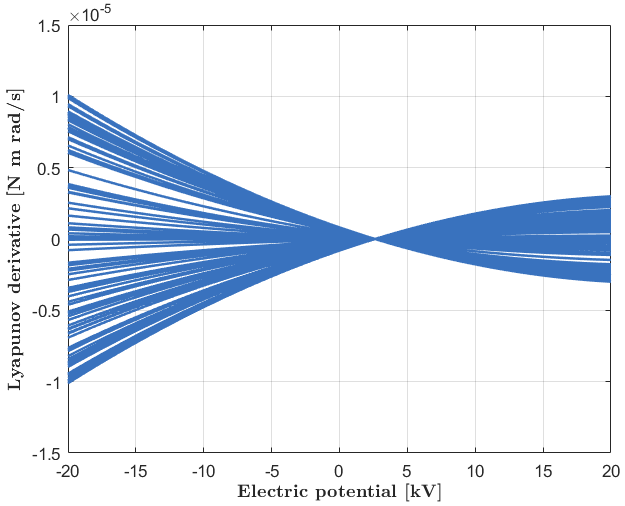

Figure 4.2: Lyapunov derivative variation with imposed potential for first 100 time steps

So, at each time step, the controller computes the resulting $\dot{T}^*$ for positive and negative imposed potential, selecting the one that ensures a negative value of $\dot{T}^*$, if neither of the two potentials grant the desired negative derivative, the controller sets both potentials to zero in order to avoid any possible increase of the kinetic energy of the system.
This only works as long as the controller is able to correctly predict the torque, if the prediction is off by a big enough value the debris kinetic energy could actually increase, leading to instability in the system.
This can be easily understood by adding and subtracting the computed Lyapunov derivative $\dot{T}^*$ to the real kinetic energy derivative:

$$T = \frac{1}{2}\boldsymbol{\omega}^T[J]\,\boldsymbol{\omega} \tag{4.3}$$

$$\dot{T} = \boldsymbol{\omega}^T[J]\,\dot{\boldsymbol{\omega}} = \boldsymbol{\omega}^T\boldsymbol{L} = \boldsymbol{\omega}^T(\boldsymbol{L} + \boldsymbol{L}^* - \boldsymbol{L}^*) = \boldsymbol{\omega}^T\boldsymbol{L}^* + \boldsymbol{\omega}^T\boldsymbol{\epsilon}_L \tag{4.4}$$

The real kinetic energy derivative consists of a first term that is negative because the controller ensures so, and a second one that depends on the error in torque estimation $\boldsymbol{\epsilon_L}$, this could either be negative or positive depending on the error and could, if bigger than the first term, bring the kinetic energy derivative up to positive values.
Nevertheless, the torque estimation is good enough if an appropriate number of spheres is set, to avoid this from happening. It can also be seen that if the

expected torque is high, the margin for error is also higher, so systems where the torques generated are higher can ensure a correct de-tumbling with higher error values. This means that larger objects may take longer to de-tumble because of the bigger inertia but also are more stable to errors in the estimation of torques, also this holds true for different torques components in the same object. For example in the case of the cylindrical debris, the rotations around the symmetry axis $\boldsymbol{b_3}$ should be less stable, because the torques generated are very low.
This hypothesis is later confirmed by the results obtained in chapter 6.

The dynamical system presented is simple yet effective for the analysis that has to be performed. Thanks to its modular structure the cases that can be analyzed are countless and this will help greatly in ensuring a correct behavior of the de-tumble in many different conditions. Moreover, the control law employed is general and can be applied to any possible scenario, its effectiveness only depends on the precision of the input parameters. The better the data available, the better the control effect is going to be, leading to faster de-tumbling and smaller residuals. In the next chapter the first results are going to be presented, these include the ideal case with different precision of the SMSM, once it has been shown that the system can handle these basic cases, uncertainties will be added.

Chapter 5

Ideal Case Results

The method developed has been applied initially to the simple geometry case with a cylindrical debris of height 3 m and radius 1 m and spherical service spacecraft of radius 2 m, to compare the results with the ones obtained with the VMSM in previous papers [26]. Once that is done, a different and more complex geometry of the service spacecraft has been considered. The same initial conditions have been used here and thruought the rest of cases analyzed, all the parameters used are provided in appendix.
In order to select the appropriate amount of spheres for the two objects, the transversal and symmetry axis torques have been computed for different spheres counts, the procedure for the box panel and cylinder geometry generated the next two figures:

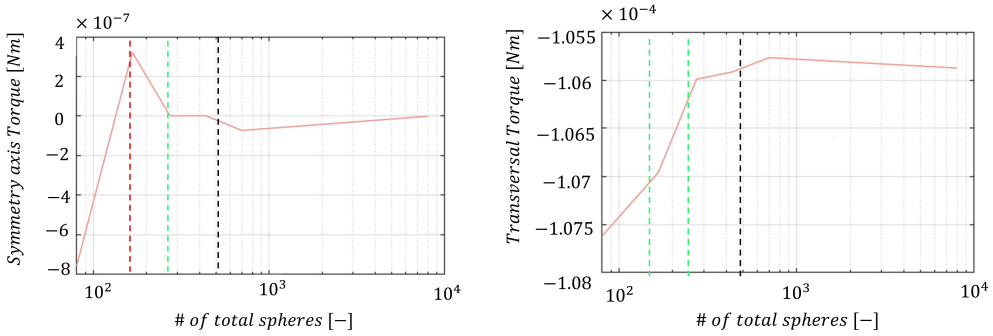

(a) Symmetry axis torque

(b) Transversal axis torque

Figure 5.1: Torque on the debris for different spheres count

As it can be seen, the torque computed stays within 2 % of the truth value for the transversal torque after more than 100 spheres are considered, but it can change considerably for the symmetry axis one.
Three different spheres count are selected in the following simulations, one for the physics modeling of the system and two different ones for the controller.

These are highlighted in Figure 5.1: as it can be seen the physics sphere count (in black) gives very similar results to the truth solution considered and both the controller models give transversal torque results within 1% of the truth solution (green lines in fig 5.1b). On the other hand, the symmetry axis torque results varies considerably between the two sphere counts chosen (green and red lines in fig 5.1a). This has been done in order to obtain some insight in the robustness of the system and how it behaves when the spheres considered have not been chosen correctly, this will be showed in the next sections and in chapter 6.

5.1 Deep space condition

In these first two cases the same number of spheres have been used in the physics model, 112 for the debris and 100 for the service, also the objects are at 10 m distance, with the debris fixed on the axis $\boldsymbol{j}$ (less spheres are necessary for this simpler geometry than in the box panel service case).

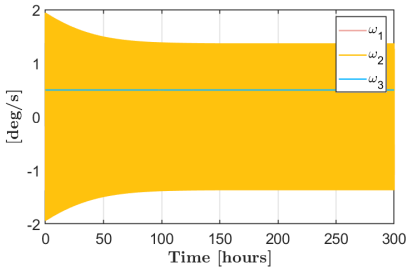

(a) Angular Velocity - VMSM Controller

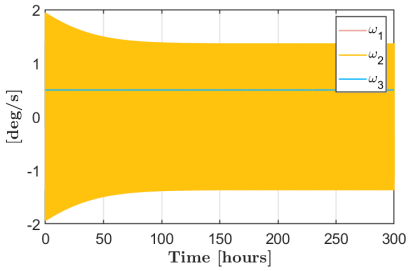

(b) Angular Velocity - SMSM Controller

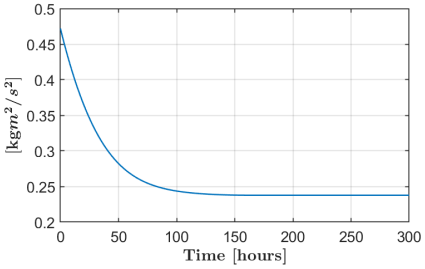

(c) Kinetic Energy - VMSM Controller

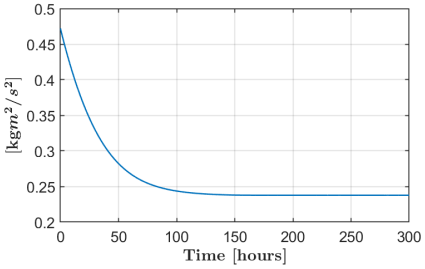

(d) Kinetic Energy - SMSM Controller

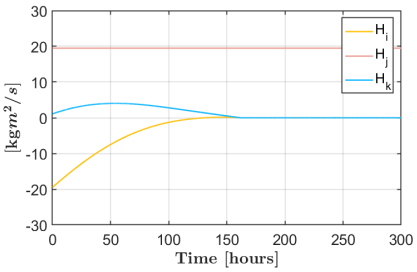

(e) Angular Momentum - VMSM Controller

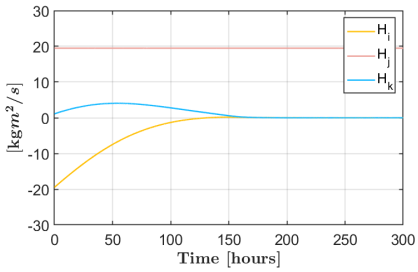

(f) Angular Momentum - SMSM Controller

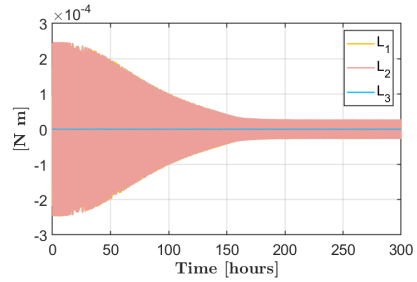

(g) Torque - VMSM Controller

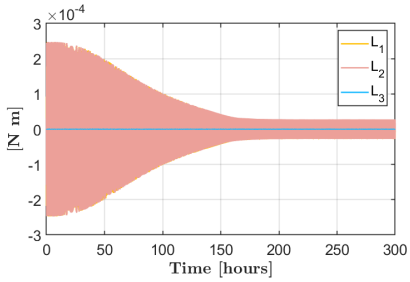

(h) Torque - SMSM Controller

Figure 5.2: Spherical service and cylindrical debris for VMSM controller and SMSM controller with 56 spheres debris and 60 spheres service

The results obtained are consistent with the previous experience, with the debris' kinetic energy decreasing monotonically until the only component of angular momentum remaining is the one along the $\boldsymbol{j}$ axis, thus along the line that links service and debris. Using an SMSM model for the controller, instead of a VMSM does not seem to influence the results obtained, so in this case the SMSM does not provide any particular advantage. This confirms the validity of the VMSM when dealing with simple shapes, since it gives the exact same results.
For the box and panels service spacecraft case depicted in Fig.3.4a:

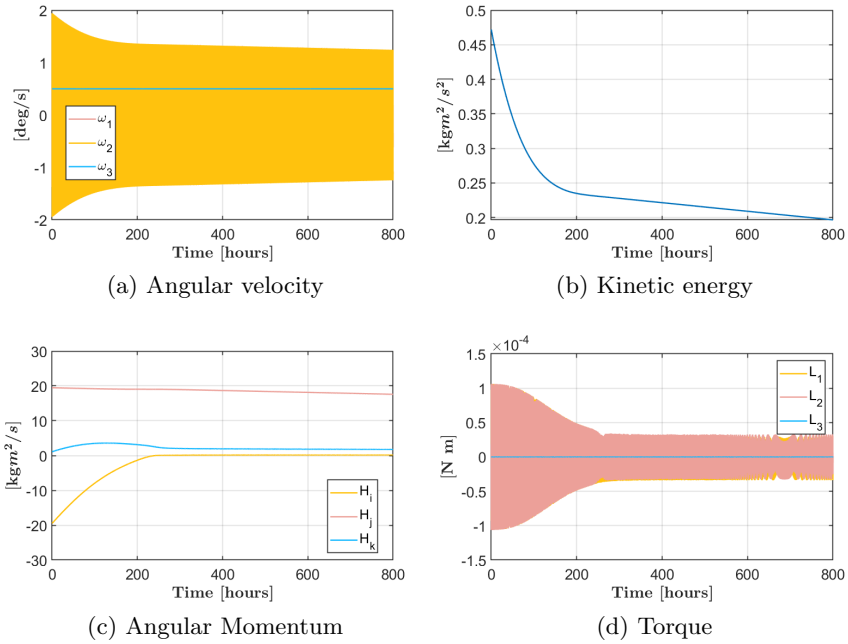

(a) Angular velocity

(b) Kinetic energy

(c) Angular Momentum

(d) Torque

Figure 5.3: Satellite service and cylindrical debris, respectively 68-56 spheres controller (red line in figure 5.1a), 160-112 spheres physics

Using the lower sphere count model does not cause any problems in the de-tumble and the system behaves correctly. Also the angular velocity of the debris does not stay constant after the initial decrease but continues to fall very slowly in time, also the component of angular momentum H_j is not constant anymore even if the time it would take to go completely to zero is in the order of months/year (the simulation time in Fig.5.3 is more than double the one in Fig.5.2). This demonstrates that the controller is able to utilize the small torques generated around $\boldsymbol{j}$ by the geometry and induced effects, effectively granting an higher level of control on the debris.

5.2 Orbit case

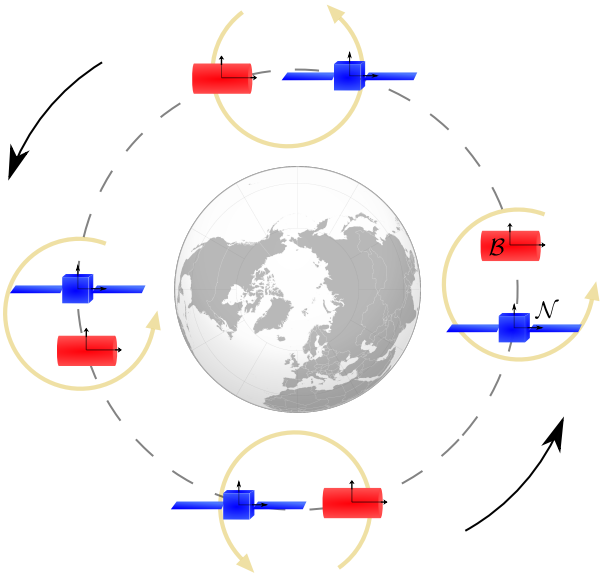

Figure 5.4: Debris and service spacecraft in a leader follower configuration

Nevertheless this effect is not exploitable given the long times it takes to bring the kinetic energy down. Moreover in the case of a GEO system, the two bodies are not fixed in the inertial frame, but are in an orbit around the equator that causes a rotation of the two frames of reference, as it can be seen in Fig. 5.4. Since the frame $\mathcal{N}$ is considered fixed in the relative system, the body frame $\mathcal{B}$ completes a rotation around it with each completed orbit, thus the whole debris rotates in the $\boldsymbol{i} - \boldsymbol{j}$ plane with an angular speed of $360/24\ deg/h$. This is modeled in the system by moving the origin point of $\mathcal{B}$, and thus the coordinates of the spheres of the debris, around the vector $\boldsymbol{k}$, at a constant distance d.

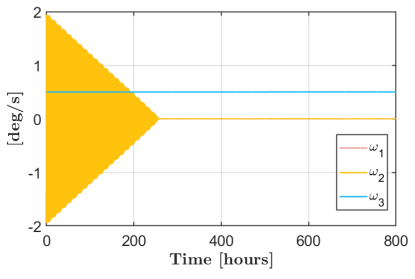

(a) Angular velocity

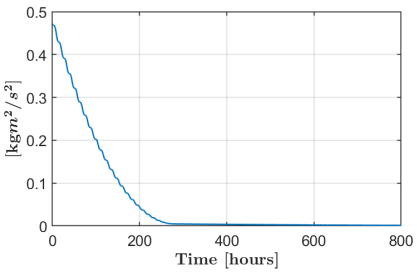

(b) Kinetic energy

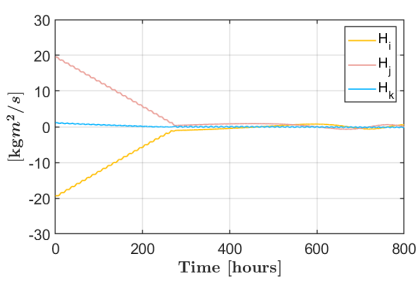

(c) Angular Momentum

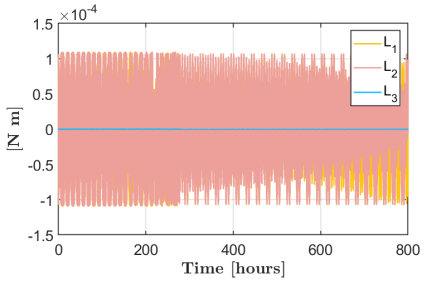

(d) Torque

Figure 5.5: Same spheres as Fig.5.3 but the debris completes a rotation around the service every 24 hours

Thanks to this, the angular momentum components H_i and H_j decrease uniformly, the total de-tumble time is reduced, also bringing the residual angular velocities $\boldsymbol{\omega_1}$ and $\boldsymbol{\omega_2}$ to zero. Also it can be seen how using the low sphere count controller model the system is still able to handle the de-tumbling effectively. The symmetry axis component $\boldsymbol{\omega_3}$ is not affected though, the reason can be found in the small magnitude of the torques around this axis, around 5 10^{-7} Nm compared to the 1 10^{-4} Nm around the other ones. Since the torque is so low, the error in torque estimation $\boldsymbol{\epsilon}_L$ (that is in the order of 10^{-6} Nm) may prevent the de-tumbling from happening.
If this is true, then reducing the error $\boldsymbol{\epsilon}_L$ may lead to an effect on the symmetry axis rotations too, this can be accomplished by utilizing a better model for the controller. Using the increased sphere count (green line in figure 5.1a) is not enough though; no significant effect is noticeable on the symmetry axis angular speed. Even using the same sphere model for both controller and physics, thus assuming a complete knowledge of the system (which is of course not possible), the following plots are obtained:

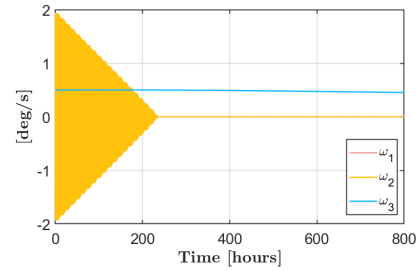

(a) Angular velocity

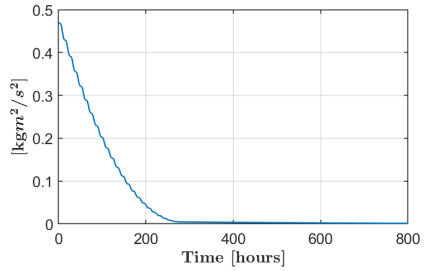

(b) Kinetic energy

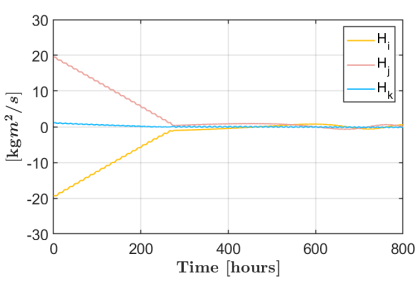

(c) Angular Momentum

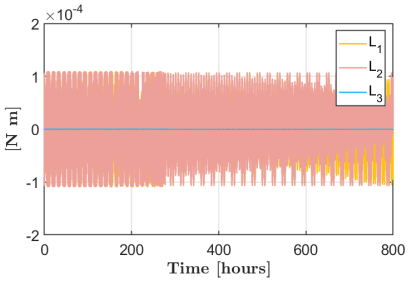

(d) Torque

Figure 5.6: System with 160-112 spheres for both controller and physics

$\boldsymbol{\omega_3}$ barely decreases from 0.5 deg/s to 0.455 deg/s in 33 days, at this rate it would take one year to fully detumble the debris and that is assuming perfect knowledge of the system, which is not possible to have. Thus even an SMSM based system is not able to fully detumble a perfectly axial-symmetric debris, in a reasonable time frame.
It should be noted how it has been demonstrated in previous studies that the relative orbit between the two bodies can influence the performances of the de-tumbling, and there is a way to exploit this in order to obtain better results. In [44] an optimizer is setup to select, at each time step, the relative orbit of the service spacecraft around the debris that maximizes the obtainable torque and thus decreases the total de-tumbling time. In the case of the study it was found that the best orbit possible is the one that keeps the position vector of the service as perpendicular as possible to the angular momentum $\boldsymbol{H}$ of the debris. This is because, with the simple geometries and models considered, that was the condition that maximizes the torque on the debris. The solution obtained was able to give better results than a simple leader follower condition without any change in absolute distance or imposed potentials.
In the case of this thesis the same approach could be employed, further increasing the final performance of the system. For simplicity, this was not included since it can be considered as an added bonus that does not influence the validity of the cases analyzed.

5.3 Mixed precision models

As stated previously, the mesh generation procedure is customizable to obtain whatever precision of the SMSM is needed, even not heterogeneous ones are possible. With this in mind, it could be interesting to examine how having a mixed precision SMSM model, changes the behavior of the system. Is it possible to increase the precision of the results by increasing the number of spheres in a portion of the model?
A lower error could lead to an effect on the $\boldsymbol{\omega_3}$ residual or an improvement in the de-tumbling time of the other two. In this next case the debris SMSM is changed, the half closer to the debris is described with the same spheres as the physics model, as depicted in Fig. 3.1c (an ideal condition).

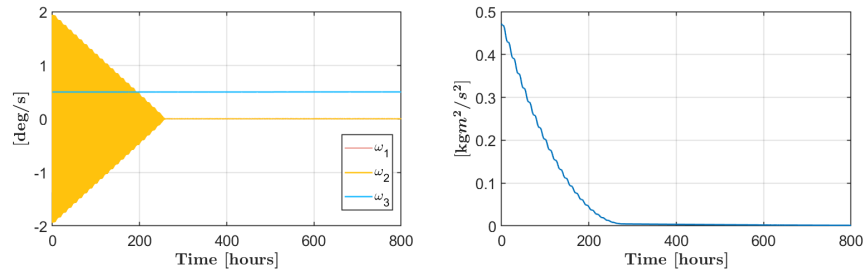

(a) Angular velocity

(b) Kinetic energy

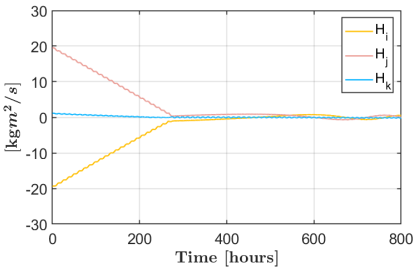

(c) Angular Momentum

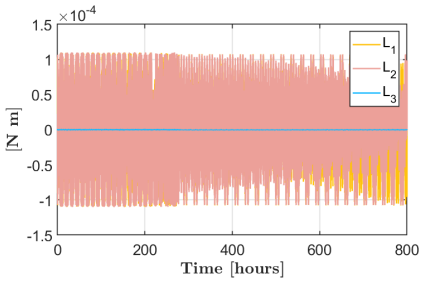

(d) Torque

Figure 5.7: Controller has the reduced precision model for the debris with 56 spheres but the service spacecraft is modeled with the mesh in Fig.3.1c, 127 spheres.

As it can be seen there is no visible effect in the symmetry axis rotations or the de-tumbling time. It means that the increase of precision granted is too low to really have any effect in the performances of the system. This should not be a surprise, given that even using the maximum precision possible for the controller model (Fig.5.6) was not enough to bring the total de-tumbling time to a feasible value.

The errors ϵ_L for both this mixed and the standard case can be seen here:

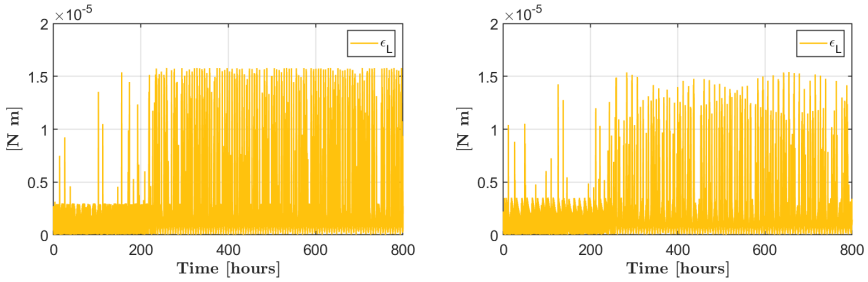

(a) Error for standard case in Fig.5.5 (b) Error for mixed case in Fig.5.7

Figure 5.8: Errors for the standard and mixed mesh.

As it can be seen, for the case analyzed there is no improvement in the maximum error obtained, only a decrease in the times the maximum error is reached which is still a good result. It may be due to the relatively small size of the system; in a case with bigger objects, a mixed model could prove more useful to decrease the total number of spheres required to describe the bodies and still get precise results. Most objects in GEO are indeed much bigger than the ones considered in this study and are usually in the order of 50 or more meters in length, so the mixed meshes may be necessary in some cases.

During this chapter it was shown how the system created is able to correctly handle different conditions and always bring the system to a minimum in kinetic energy. In particular it was shown how the SMSM model does not bring any considerable benefits for simpler cases but can help describe the induced effects in a more complex geometry like the box and panel service case. These induced effects are very small and hard to describe correctly and even in the case of a perfect torque knowledge their magnitude is so small that a full de-tumble would take more than a year.
The rotation of the debris around the service, caused by the leader follower orbiting configuration, allows for a much faster and complete detumbling of the two transverse axis spins. None of the alternatives analyzed leads to a substantial decrease in the angular velocity around the symmetry axis, even in the case of ideal precision models.
The next chapter will move to analyzing the robustness of the system to uncertainties, an aspect that was not considered in previous studies.

Chapter 6

Robustness analysis

An important goal of this study is to obtain a numerical quantification of the effect of system parameters uncertainty, on the stability and performance of the de-tumbling. Previously, it was shown how this can be obtained for the error in torque estimation $\boldsymbol{\epsilon}_L$, but this can be further expanded by adding different contributions to the errors like solar radiation pressure or, most importantly, errors in the estimated Inertia matrix and center of mass of the debris.
Both J2 disturbances and magnetic torques are not included since they are usually negligible in the GEO regime, due to the high altitude of the orbit.

6.1 Solar radiation pressure

The effect of solar radiation pressure is modeled as a separate torque $\boldsymbol{L}_{\text{srp}}$ that acts on the debris. This is done in a separate block that takes as an input the position and attitude of the debris and uses it to compute the disturbance. Since there is no simple way to obtain the force resulting from the pressure distribution on the curved surface of the cylinder, the debris is modeled as an octagonal prism.

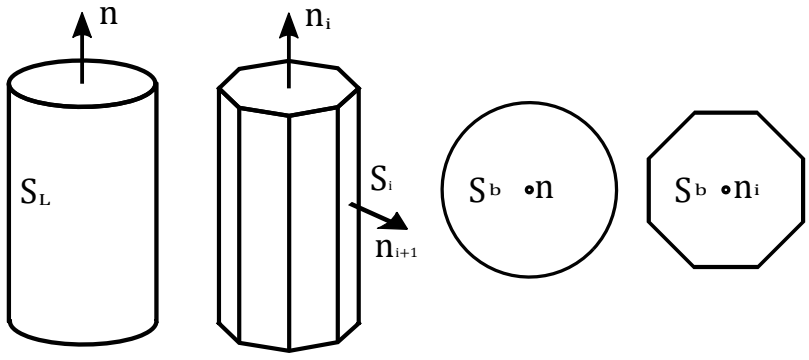

Figure 6.1: Cylinder debris modeled as equivalent octagonal prism

The prism has the same base area S_b as the cylinder and each side is sized such as the summation of all the 8 lateral rectangles is the same as the lateral surface S_L of the cylinder. This results in dimensions that do not fit together since the edges of the octagon are shorter than the rectangles smaller sides. It does not matter though since only the area S_i and the direction vector $\boldsymbol{n_i}$, of each i face, are important.
Indeed the torque component given by each surface is given by:

$$\boldsymbol{F_{Si}} = P_s S_i (\boldsymbol{S} \cdot \boldsymbol{n_i})[(1-\rho_S)\boldsymbol{S} + (2\rho_S(\boldsymbol{S} \cdot \boldsymbol{n_i}) + 2/3\rho_D)\boldsymbol{n_i}] \tag{6.1}$$

$$\boldsymbol{F_{Ei}} = P_e S_i (\boldsymbol{h} \cdot \boldsymbol{n_i})[(1-\rho_S)\boldsymbol{h} + (2\rho_S(\boldsymbol{h} \cdot \boldsymbol{n_i}) + 2/3\rho_D)\boldsymbol{n_i}] \tag{6.2}$$

$$\boldsymbol{L_{SRPi}} = \boldsymbol{r_i} \times \boldsymbol{F_S i} + \boldsymbol{r_i} \times \boldsymbol{F_E i} \tag{6.3}$$

Two force components are computed on each i surface: the force resulting from the Sun radiation $\boldsymbol{F_S}$ and the one from the Earth albedo $\boldsymbol{F_E}$. these two components come respectively from the Sun direction $\boldsymbol{S}$ and Earth horizon $\boldsymbol{h}$, both computed from Ephemeridies considering the initial date of the simulation to be the 21$^{\text{st}}$ of June 2019.
The radiation pressures P_s and P_e, are obtained by using models that take into account both the altitude of the orbit and eclipses caused by the Earth and atmosphere blocking the Sun rays to the debris. Also the direction of the surface normal $\boldsymbol{n_i}$ is taken into account thanks to the cosine law, so that the faces that are in shadow do not contribute to the total. The resulting force is then vectorially multiplied by the surface center position vector $\boldsymbol{r_i}$ to compute the torque L_{SRP}.
The disturbance torque is several order of magnitudes lower than the control torque provided by the system and no effect is noticeable in the performance of the de-tumbling. For these reasons the result plots are not given here as they would be identical to the ones in Fig. 5.5.

6.2 Center of mass deviation

This is the first time that this kind of analysis is conducted for an electrostatic de-tumbling system, the effects of center of mass deviation have been analyzed before, but only in terms of controllability of the system [45] so it was not stated what would happen if the center of mass of the debris is different from the one the controller expects.
This can easily be modeled in the system by adding a contribution to the torque in Eq.3.10 :

$$\boldsymbol{L} = \sum_{j=1}^{M} (\boldsymbol{r}_{j|b} - \boldsymbol{\delta}) \times \boldsymbol{F}_j = \sum_{j=1}^{M} \boldsymbol{r}_{j|b} \times \boldsymbol{F}_j + \sum_{j=1}^{M} (-\boldsymbol{\delta}) \times \boldsymbol{F}_j = \boldsymbol{L}_I + \boldsymbol{L}_d \tag{6.4}$$

So the real torque is now composed by two contributions, the first $\boldsymbol{L}_I$ given by the ideal position of the center of mass and the second one $\boldsymbol{L}_d$ given by its deviation, only present in the physics model and not in the controller.
Also the expected torque $\boldsymbol{L}^*$ and the error in torque estimation $\boldsymbol{\epsilon}_L$, can be changed to $\boldsymbol{L}_I^*$ and $\boldsymbol{\epsilon}_I$ for clarity since they refer to the estimate of the ideal torque $\boldsymbol{L}_I$ with respect to the ideal center of mass (CM).
This way it is easy to see that the kinetic energy derivative (Eq. 4.4) now has the same contribution as before regarding the ideal torque and another one given by the deviation in the CM:

$$\dot{T} = \boldsymbol{\omega}^T \boldsymbol{L}_I^* + \boldsymbol{\omega}^T (\boldsymbol{\epsilon}_I + \boldsymbol{L}_d) \tag{6.5}$$

In order to better understand how different deviations affect the system, simulations with $\boldsymbol{\delta}$ components only along one axis at the time have been performed. Again the specifics of the parameters used can be found in appendix:

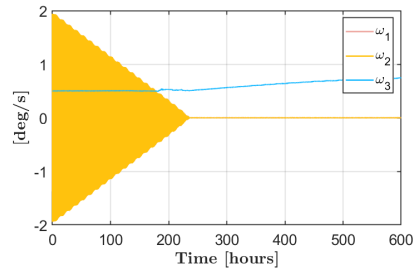

(a) Angular Velocity - $\boldsymbol{b}_1$ deviation

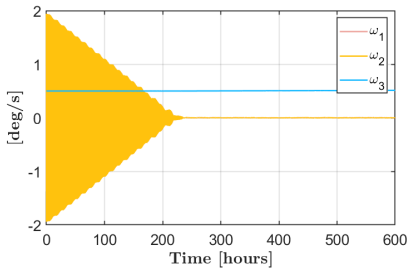

(b) Angular Velocity - $\boldsymbol{b}_3$ deviation

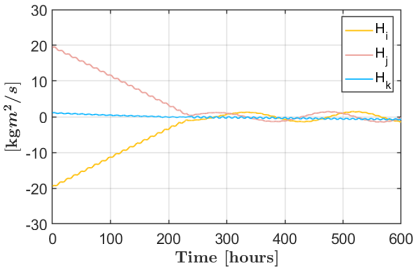

(c) Angular Momentum - $\boldsymbol{b}_1$ deviation

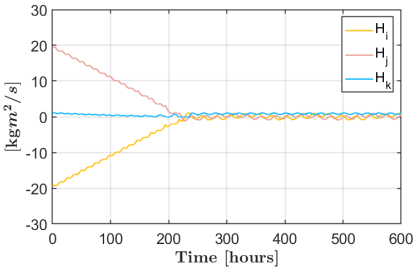

(d) Angular Momentum - $\boldsymbol{b}_3$ deviation

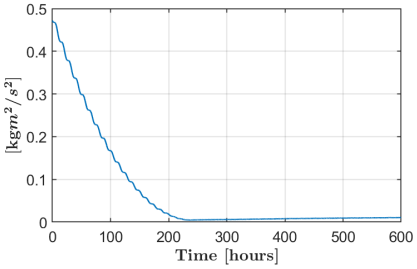

(e) Kinetic Energy - $\boldsymbol{b}_1$ deviation

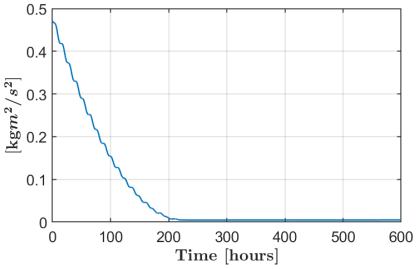

(f) Kinetic Energy - $\boldsymbol{b}_3$ deviation

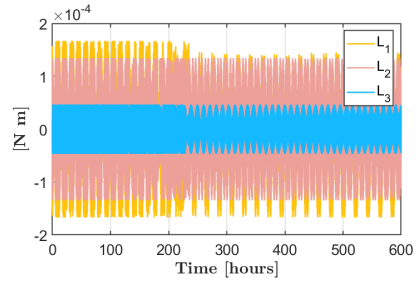

(g) Torque - $\boldsymbol{b}_1$ deviation

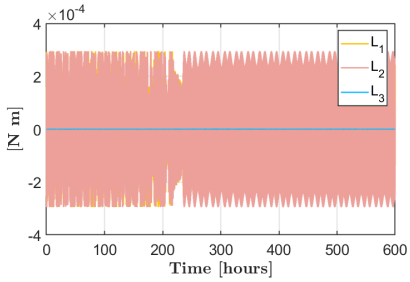

(h) Torque - $\boldsymbol{b}_3$ deviation

Figure 6.2: Stability analysis for center of mass deviation along $\boldsymbol{b}_1$ in the first row and $\boldsymbol{b}_3$ in the second one, using the higher sphere model

As it can be seen the system is not significantly affected by the deviations of the center of mass position, but there is still a small increase in $\boldsymbol{\omega}_3$ that if not appropriately handled could lead to unstable behavior.
In fact, if the simulation is repeated with the lower sphere count for the controller model:

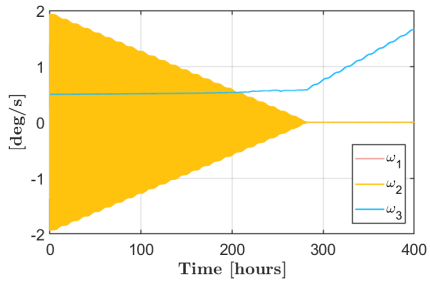

(a) Angular Velocity - $\boldsymbol{b}_1$ deviation

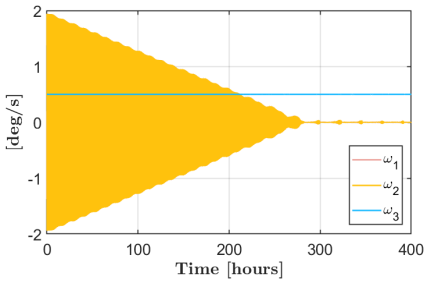

(b) Angular Velocity - $\boldsymbol{b}_3$ deviation

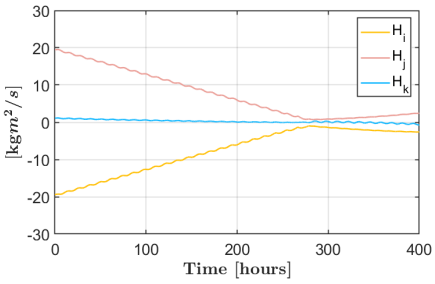

(c) Angular Momentum - $\boldsymbol{b}_1$ deviation

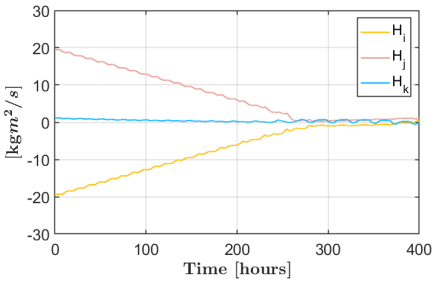

(d) Angular Momentum - $\boldsymbol{b}_3$ deviation

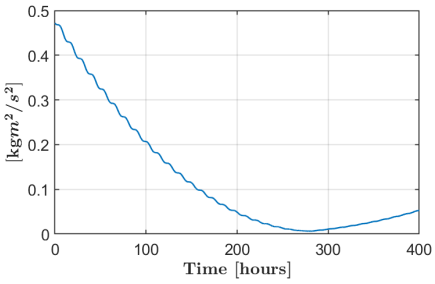

(e) Kinetic Energy - $\boldsymbol{b}_1$ deviation

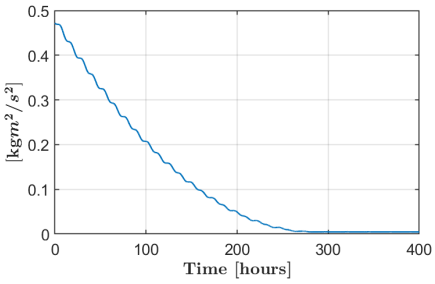

(f) Kinetic Energy - $\boldsymbol{b}_3$ deviation

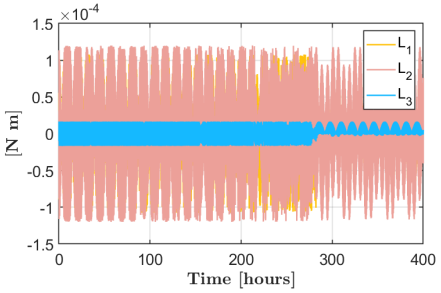

(g) Torque - $\boldsymbol{b}_1$ deviation

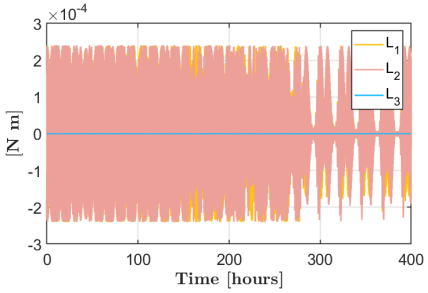

(h) Torque - $\boldsymbol{b}_3$ deviation

Figure 6.3: System with CM deviation and controller spheres of debris reduced to 56

If the center of mass is moved from the symmetry axis, the system reaches instability very quickly, even 2 cm are enough to cause unstable behavior of $\boldsymbol{\omega}_3$, this demonstrates how sensitive the rotation around this axis can be to the model used, so great care must be taken when selecting the sphere count to use.
As expected the system is much more stable to deviations of the center of mass along the symmetry axis, that do not lead to instability for reasonable deviations, only the total de-tumbling time can be affected by big enough δ_3.
Moreover it is interesting to see how the increase in angular velocity happens only after the other two components have been brought to almost zero. This is a result of the structure of the controller that tends to prioritize potentials that give torques around the first two axes as these also grant higher torques on the debris thus decreasing the kinetic energy the most. Once both these components are brought to zero the controller tries to utilize the small torques around $\boldsymbol{b}_3$, given only by the induced effects and small asymmetries of the charge distribution, to further decrease the kinetic energy but since the resulting torque is different because of the deviation component, the angular velocity can end up increasing uncontrollably, as the system has no way of dealing with this effect.

6.3 Inertia parameters uncertainty

In a real case, if the center of mass is in a different position than expected, then also the rotational inertia of the body is going to change. This is the next uncertainty included in this study, to try and understand the effect of a non axis symmetric mass distribution, on the system dynamics.
For simplicity it is assumed that the unexpected change in inertia and CM position is given by a point mass propellant tank m_p, positioned on the axis $\boldsymbol{b_1}$ and then on $\boldsymbol{b_3}$.

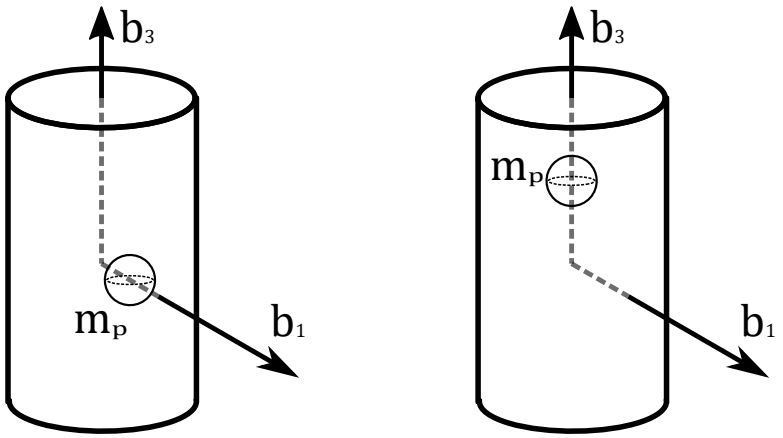

Figure 6.4: Tank position in the cylindrical debris, in the two cases considered

The value and distance from the center of the tanks have been picked to give the exact same CM deviations of Fig.6.3. For the deviation along $\boldsymbol{b_1}$ the tank has a mass $m_p = 100$kg and a distance of 0.55 m, for the one along $\boldsymbol{b_3}$ it is $m_p = 200$kg at a distance of 1.2 m. Then the change in inertia change on each component is obtained as:

$$I_i = I_i^* + m_{\text{cyl}}\delta_j^2 + m_p(\delta_j - r_{pj})^2 \tag{6.6}$$

So the real Inertia component I_i is given by the assumed ideal one I_i^*, plus a contribution given by the change in CM itself and one given by the point mass tank in $\boldsymbol{r_p}$. The two cases presented below have an inertia matrix of respectively $[J] = diag[812.5\ 840\ 152.5]$ kg m^2 and $[J] = diag[1052.5\ 1052.5\ 125]$ kg m^2:

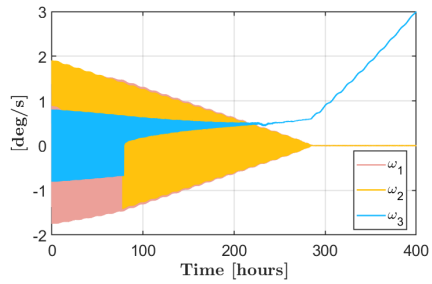

(a) Angular Velocity - $\boldsymbol{b}_1$ deviation

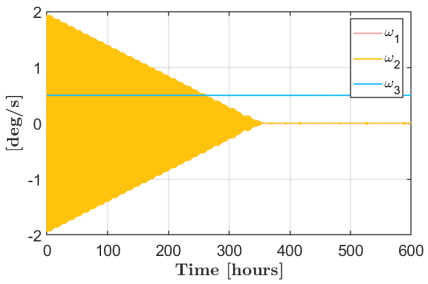

(b) Angular Velocity - $\boldsymbol{b}_3$ deviation

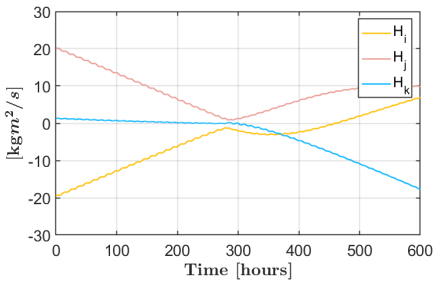

(c) Angular Momentum - $\boldsymbol{b}_1$ deviation

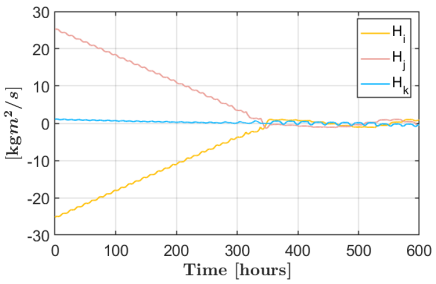

(d) Angular Momentum - $\boldsymbol{b}_3$ deviation

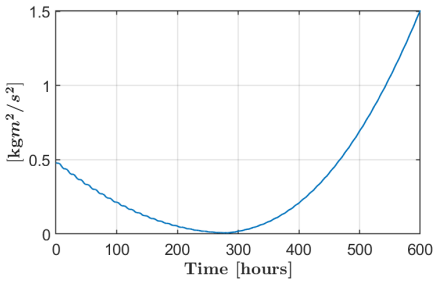

(e) Kinetic Energy - $\boldsymbol{b}_1$ deviation

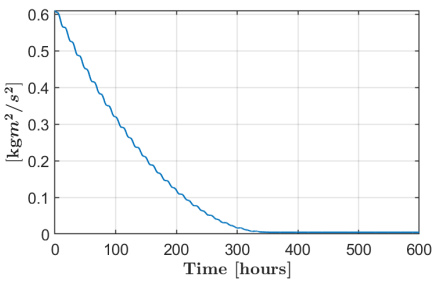

(f) Kinetic Energy - $\boldsymbol{b}_3$ deviation

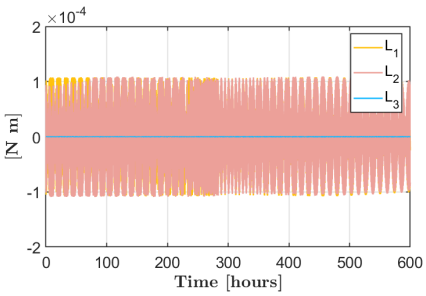

(g) Torque - $\boldsymbol{b}_1$ deviation

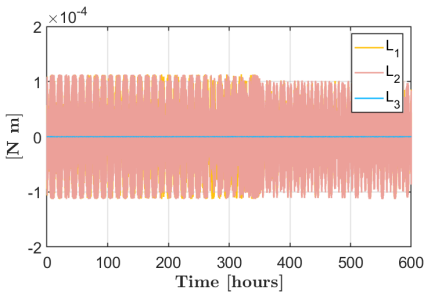

(h) Torque - $\boldsymbol{b}_3$ deviation

Figure 6.5: System with same spheres as Fig.6.3
but inertia variations are included too

An unexpected mass along $\boldsymbol{b_1}$ has a substantial effect on the dynamics of the cylinder: since the debris is not axis-symmetric anymore, ω_1 and ω_2 do not follow the same evolution as before, also ω_3 can be seen oscillating in the first part, before settling and returning to normal unstable behavior. It can be noted that, while the evolution of the rotations is much more unpredictable, thus more dangerous, the total de-tumbling time and residual is not affected at all, so in the end the performance stays the same.
The opposite happens in the case of a deviation along $\boldsymbol{b_3}$: as it can be seen the rotations are still symmetrical and stable, since the debris is still axis-symmetric, but the total de-tumbling time is around 30% higher than before since the inertia has increased.

6.4 Improving the robustness

In the previous sections it was highlighted how the system can be hindered by various uncertainties, and how these can have an effect on both performances and safety of the operation. In particular the monotonic increase of the angular velocity around the symmetry axis is the most concerning. This could lead to an extreme increase in the total kinetic energy of the debris, rendering any future de-orbiting attempts impossible.
Two main solutions could be employed:

- Since the unstable behavior manifests itself only after $\boldsymbol{\omega}_1$ and $\boldsymbol{\omega}_2$ are brought to zero, the controller could be setup to turn itself off after the components of kinetic energy ($T_i = I_i {\omega_i}^2$) that depend on those two are decreased below a certain portion of the third one (T_1 and $T_2 < k\ T_3$). This way the system is able to de-tumble most of the debris kinetic energy without incurring in any unstable behavior.

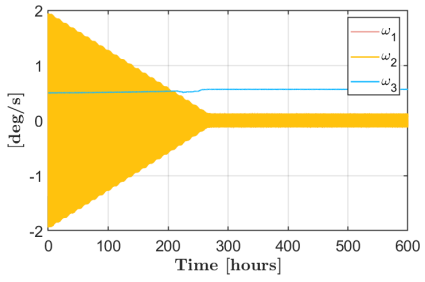

Figure 6.6: Angular velocity with shutoff control in unstable case

This strategy is simple and effective but has some significant issues, first of all it completely removes any possible control authority on the symmetry axis which could be a problem if the angular velocity around it is too big to be acceptable. Also it relies on the ability of the system to recognize which axis would yield the lowest torque and thus be more susceptible

to unstable behavior. This is not a simple task to accomplish and could require more work than reasonably possible, to setup correctly.

- A better alternative would be to estimate the deviation torque $\boldsymbol{L}_d$ and other disturbances in the system and use this to predict instabilities and avoid them. Easier said than done, there is a method developed in the last decade called Active Disturbance Rejection Control (ADRC) that has already proved very useful in many applications [29–32]. This has been found to be very effective in the cases analyzed and a more in depth explanation of its structure is given in the next section.

6.5 Active Disturbance Rejection Control

The birth and large-scale deployments of the powerful yet primitive proportional–integral–derivative (PID) control law dates back to the period of the 1920s–1940s in response to the pressing demands of industrial automation before, during, and particularly after World War II.
Its merit of simplicity in the analog electronics era has turned into a liability in the digital control one as it cannot fully take advantage of the new compact and powerful digital processors.

Reference [30] suggests that there are four fundamental technical limitations in the existing PID framework, and proceeds to propose the following technical and conceptual solutions: 1) a simple differential equation to be used as a transient profile generator; 2) a noise-tolerant tracking differentiator; 3) the power of nonlinear control feedback; and 4) the total disturbance estimation and rejection.

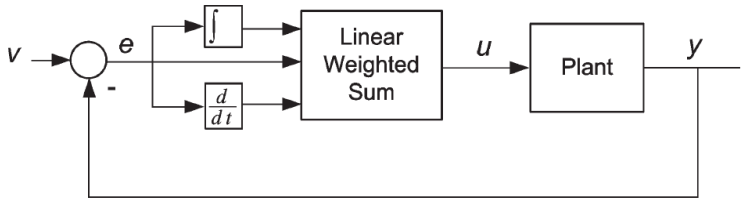

Figure 6.7: PID architecture, image taken from [30]

Together, these new tools combine to form the backbone of a new synthesis of digital control law that is not dependent on an accurate and detailed dynamic model of the plant and is extremely tolerant of uncertainties and simple to use. This is called active disturbance rejection control or ADRC.
As the name suggests, the PID control depends on the difference between the output of a system and its desired value, the derivative and integral of this error itself.

$$u = k_p\ e + k_d\ \dot{e} + k_i \int_0^t e\ \mathrm{d}\tau \tag{6.7}$$

The gains k can be found, analytically when the model is given or by trial and error when it is not. Although such simplicity and the ease of tuning could very well be behind the popularity of PID, they also mark its fundamental limitations. A hand tuning method, based on trial and error, can be hard to set for complex systems, where there is not an analytical function that links input (in the case of the de-tumbling system, the potential imposed on the service craft) and output(debris kinetic energy).

In the case of the ADRC, the focus is not on completely understanding how the system relates input and output and use this to get the desired results, but on directly anticipating and canceling the disturbance itself. Once the disturbance is handled the system can be controlled as usual, using the selected control law (like the Lyapunov optimal law used in this thesis)

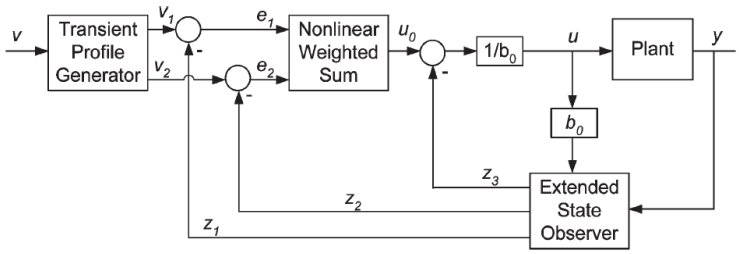

Figure 6.8: ADRC architecture, image taken from [30]

This control strategy is effective in cases where the disturbances in the system are uncertain, which is the case of debris de-tumbling. These are often objects on which very little information is available, apart from what can be observed from the outside. More insight could be obtained if the objective of the de-tumble is a known satellite or spacecraft so the blueprints and internal structure can be analyzed but even then there could be some unexpected amount of fuel left in some tanks or some parts of the structure could be missing.
In general it is impossible to know exactly all proprieties of the debris and in particular the position of the center of mass and the inertia. The ADRC works by using an extended state observer to reconstruct the differences between the modeled system and the real one, by lumping all the differences together as a single disturbance torque.

Moreover, by splitting the inertia in the expected and uncertain parts it can be written:

$$\begin{aligned}
[J]\dot{\boldsymbol{\omega}} &= ([J]^* + [\Delta J])\dot{\boldsymbol{\omega}} = ([J]^* + [\Delta J])\boldsymbol{\omega} \times \boldsymbol{\omega} + \boldsymbol{L} \\
[J]^*\dot{\boldsymbol{\omega}} &= [J]^*\boldsymbol{\omega} \times \boldsymbol{\omega} + \boldsymbol{L}_I^* + \underbrace{[\Delta J]\boldsymbol{\omega} \times \boldsymbol{\omega} - [\Delta J]\dot{\boldsymbol{\omega}} + \boldsymbol{L}_D + \boldsymbol{\epsilon}_I} \\
[J]^*\dot{\boldsymbol{\omega}} &= [J]^*\boldsymbol{\omega} \times \boldsymbol{\omega} + \boldsymbol{L}_I^* + \boldsymbol{d}
\end{aligned} \tag{6.8}$$

This way, the real system can be described using the expected values plus an unknown $\boldsymbol{d}$ that includes all unexpected contributions to the dynamics of the system.

The extended state observed, taken from [29, 31] is given by:

$$\begin{cases} [J]^*\dot{\boldsymbol{\omega}}^* & = [J]^*\boldsymbol{\omega}^* \times \boldsymbol{\omega}^* + \boldsymbol{L}_I^* + \boldsymbol{d}^* + \beta_1(\boldsymbol{\omega} - \boldsymbol{\omega}^*) \\ \dot{\boldsymbol{d}}^* & = \beta_2(\boldsymbol{\omega} - \boldsymbol{\omega}^*) \end{cases} \tag{6.9}$$

By comparing the real angular velocity $\boldsymbol{\omega}$ of the debris (given by the sensors on the service spacecraft) to the expected one $\boldsymbol{\omega}^*$, an estimate $\dot{\boldsymbol{d}}^*$ of the disturbance derivative $\dot{\boldsymbol{d}}$ is obtained, and once integrated, fed into the controller to correct the computed value of the Lyapunov function $\dot{T}^*$ that is now written as:

$$\dot{T}^* = \boldsymbol{\omega}^T(\boldsymbol{L}_I^* + \boldsymbol{d}^*) \tag{6.10}$$

Again, the controller checks the value of $\dot{T}^*$ for positive and negative service electric potential, and picks the one that gives a negative $\dot{T}^*$. There are some drawbacks in this though, because since the value of $\boldsymbol{d}^*$ is received as an input from the controller, it acts as a constant when in reality it also depends from the chosen potential.
The system is then forced to assume the value of $\boldsymbol{d}^*$ originated from the last time step of integration, generating some inaccuracies that could prove significant if the state of the objects couple changes very quickly. In the cases examined, the evolution of the system is so slow that this does not seem to hinder the efficiency of the control, regardless it is still something to take into consideration during the analysis.
This updated Lyapunov derivative when added and subtracted to the real kinetic energy derivative gives:

$$\dot{T} = \boldsymbol{\omega}^T\boldsymbol{L} = \boldsymbol{\omega}^T(\boldsymbol{L} + \boldsymbol{L}_I^* + \boldsymbol{d}^* - \boldsymbol{L}_I^* - \boldsymbol{d}^*) \tag{6.11}$$

Expanding the contributions of $\boldsymbol{L}$ and the lumped sum $\boldsymbol{d}^*$ into its components (the term $\boldsymbol{\epsilon}_I^*$ is not included since it is several order of magnitutes smaller than other components of $\boldsymbol{d}^*$ so it is not picked up by the state observer, unless the precision given is very high) and deleting the perpendicular term, it becomes:

$$\begin{aligned} \dot{T} &= \boldsymbol{\omega}^T(\boldsymbol{L}_I + \boldsymbol{L}_d + \boldsymbol{L}_I^* + \hat{\boldsymbol{d}} - \boldsymbol{L}_I^* - \boldsymbol{d}^*) \\ &= \boldsymbol{\omega}^T(\boldsymbol{L}_I^* + \boldsymbol{d}^*) + \boldsymbol{\omega}^T(\boldsymbol{L}_I - \boldsymbol{L}_I^* + \boldsymbol{L}_d - \boldsymbol{L}_d^* + [\Delta J]^*\dot{\boldsymbol{\omega}}) \\ &= \boldsymbol{\omega}^T(\boldsymbol{L}_I^* + \boldsymbol{d}^*) + \boldsymbol{\omega}^T(\boldsymbol{\epsilon}_I + \boldsymbol{\epsilon}_d + [\Delta J]^*\dot{\boldsymbol{\omega}}) \end{aligned} \tag{6.12}$$

Similarly to before there is a first term that is always negative since it is selected as such by the controller (has a value of around -5×10^{-5} kg m^2/s^2 for the case shown below) and a second one given by the estimation errors of ideal, deviation torque (10^{-7} kg m^2/s^2) and the estimated inertia uncertainty(2×10^{-5} kg m^2/s^2). The error in torque estimation depends greatly in how quickly the torque imposed changes, so it will be higher when the system switches potential very quickly. In this example, the last contribution is the most significant and the one that is most likely to degrade the performances of the system, this is a product of the way the ADRC estimates the unknown $\boldsymbol{d}$. Since it is a lumped sum there is no way to select the different contributions, so the term given by the change in inertia is present and it can not be decreased without obtaining a better knowledge of the debris mass proprieties.

The next plots show some of the cases analyzed and give a plain picture of how this improved control law is able to handle increasing deviations of the center of mass and Inertia uncertainties, again the specifics are given in appendix:

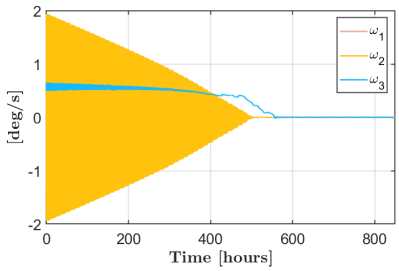

(a) $\Delta J = 5\%$ - 7.6 cm deviation

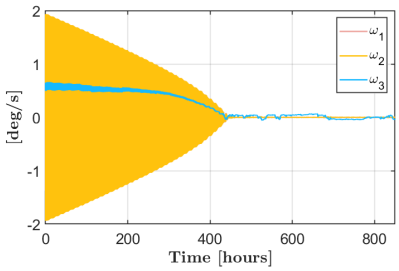

(b) $\Delta J = 5\%$ - 15.2 cm deviation

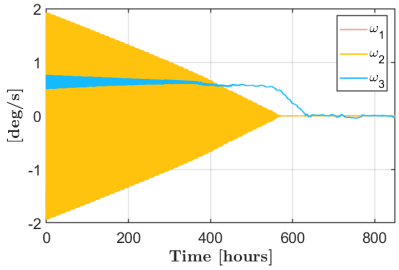

(c) $\Delta J = 10\%$ - 7.6 cm deviation

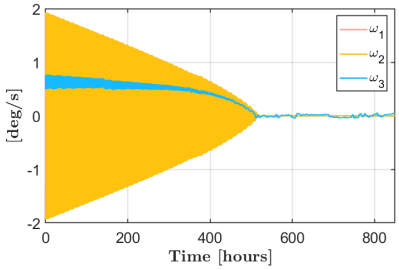

(d) $\Delta J = 10\%$ - 15.2 cm deviation

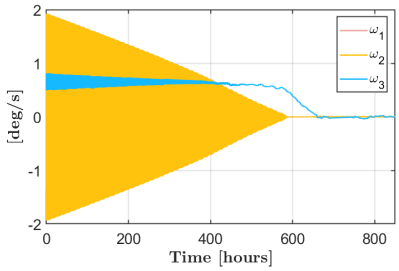

(e) $\Delta J = 12.5\%$ - 7.6 cm deviation

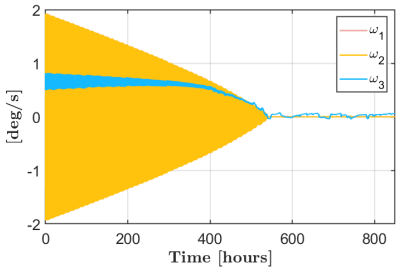

(f) $\Delta J = 12.5\%$ - 15.2 cm deviation

Figure 6.9: 68-84 spheres controller, 160-112 spheres physics with ADRC improved control

The ADRC is able to effectively detect and utilize the unexpected center of mass deviation, and the higher the deviation is, the easier it is for the system to control and de-tumble the debris. As it can be seen, all the cases on the bottom row where the deviation is double in magnitude (but has the same direction) are able to reduce the rotations along the symmetry axis faster. On the other hand the bigger the $[\Delta J]$ is, the more time the system needs to completely de-tumble the debris.

If the same deviations and inertia uncertainty are given but with the lower sphere count of Fig.6.3:

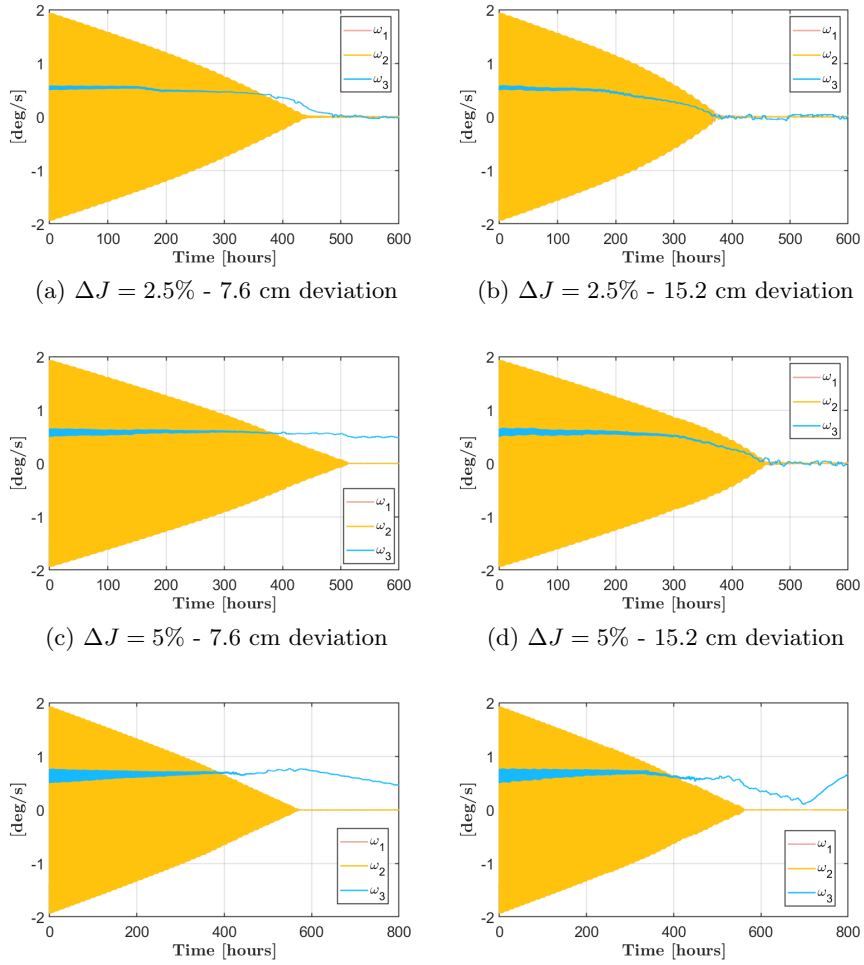

(a) $\Delta J = 2.5\%$ - 7.6 cm deviation

(b) $\Delta J = 2.5\%$ - 15.2 cm deviation

(c) $\Delta J = 5\%$ - 7.6 cm deviation

(d) $\Delta J = 5\%$ - 15.2 cm deviation

(e) $\Delta J = 10\%$ - 7.6 cm deviation

(f) $\Delta J = 10\%$ - 15.2 cm deviation

Figure 6.10: 68-56 spheres controller, 160-112 spheres physics with with ADRC improved control

The improved control is still able to grant total de-tumbling in the cases with lower inertia uncertainty, but higher $[\Delta J]$ can considerably slow down the de-tumbling and also lead to an increase in $\boldsymbol{\omega}_3$.
So while the ADRC has proved to be a powerful tool that considerably improves the robustness and performance of the system, it still necessary to select precise enough sphere models to ensure a correct behavior of the system, especially when there is no precise knowledge of the debris inertia.
It is then advisable for the service spacecraft to spend some time before the de-tumbling to analyze the free rotations of the debris and try to reconstruct

an inertia matrix with the help of LIDAR and image processing algorithms like [40–42].
Also the gains β_1 and β_2 do not need to be changed for each different use, since they only depend on the speed at which the system needs to work and that is based on the angular velocity of the debris itself.

At this point is possible to conclude that the ADCR is an exceptional tool to greatly improve the robustness and performance of the de-tumble. Being able to pick up and take advantage of small deviations in the center of mass of the debris, allows for a complete de-tumble of the spacecraft. It is reasonable to say that a small deviation of CM is likely present in most of axis symmetric debris, this means that even the worst case scenario for an electrostatic de-tumbling (axis symmetric debris), can be fully de-tumbled by taking advantage of these small deviations. This is even easier to do in the case of a non symmetric debris, where the attainable torques are all high enough to allow full controllability on all axis.
Even in the case of a imprecise sphere model, the ADRC is able to grant robustness up to 10% in inertia uncertainty, and avoid any substantial increase in angular velocity.

Chapter 7

Conclusion

7.1 Final remarks on results

The results obtained in this study show that the Surface Multi Sphere Model is an effective model to describe the charge distribution in a generic body, without any constraints on its shape. The torques and forces acting on the objects can be correctly computed at faster than real time speed if the number of spheres considered is appropriate. Using these models and the Lyapunov optimal control law, it was possible to decrease the kinetic energy of the debris, even when accounting for uncertainties and disturbances.
In particular it was showed in Chapter 5 that the system can match the same results obtained with a VMSM control based on analytical assumptions, for the simple spherical service and cylindrical debris case.
This can be seen in the next table:

Case	$\boldsymbol{\omega}_{1/2}$ **De-tumble time**	$\boldsymbol{\omega}$ **residual**
3 spheres VMSM controller	100 [h]	[1.5, 1.5, 0.5] [deg/s]
116 spheres SMSM controller	100 [h]	[1.5, 1.5, 0.5] [deg/s]

Table 7.1: Deep space spherical service case for the two Multi Sphere Models

In this case the SMSM does not bring any benefits, but this can be expected with these simple geometries, it must be kept in mind that the main advantage of the SMSM is its flexibility and simplicity of implementation. As it was described in chapter 3 the procedure to generate the SMSM model with the MOM is faster and more general than the VMSM one. These first runs were simply a way to confirm that the control law actually de-tumbles the system as desired, without relying on any analytical control function, no substantial improvements in performance were expected.

Then the analysis is moved to a box and panel service spacecraft shape, the debris is kept cylindrical since it represents on of the most common shapes in GEO and one of the hardest to de-tumble, given its axis-symmetric structure. When the debris is axis-symmetric the controllability is greatly reduced along the symmetry axis, since the system is not able to generate large enough torques. The results obtained can not be compared to a VMSM any longer since there is no previous study for this service shape, but different precision SMSM models were compared:

Case	$\boldsymbol{\omega}_{1/2}$ **De-tumble time**	$\boldsymbol{\omega}$ **residual**
124 sphere SMSM controller	150 [h]	[1.2, 1.2, 0.5] [deg/s]
272 spheres SMSM ideal	140 [h]	[1.1, 1.1, 0.5] [deg/s]

Table 7.2: Deep space box and panel service case

The main part of the kinetic energy is dissipated in 150 hours, after that the residual decreases slowly until the value above is reached in around 800 hours. It would go until zero if the simulation is left running for longer. This is faster if the model used is very precise, like in the second case that uses the same spheres for both controller and physics, but it is still too slow to be feasible in a real case. Moreover only the transversal components are decreased, no effect is present on the symmetry axis rotations.
If the rotations of the debris around the service, in a leader follower condition are included, the performances increase considerably:

Case	$\boldsymbol{\omega}_{1/2}$ **De-tumble time**	$\boldsymbol{\omega}$ **residual**
124 sphere SMSM controller	220 [h]	[≈ 0, ≈ 0, 0.5] [deg/s]
195 sphere mixed SMSM	220 [h]	[≈ 0, ≈ 0, 0.5] [deg/s]
272 spheres SMSM ideal	220 [h]	[≈ 0, ≈ 0, 0.45] [deg/s]

Table 7.3: Leader-follower configuration, box and panel service case

Now that the debris CM position is not fixed relative to the service craft's one, the two components of transversal rotations are decreased almost completely (the residual is negligible), but there is still no effect on the third symmetric component, even with a mixed mesh. Only the ideal case with a perfect charge model is able to decrease the rotations by 0.05 deg in around 800 hours. Even the ideal case would not be fast enough to achieve a full de-tumble in feasible times.

Once the performances of the system were analyzed in the nominal case, uncertainties in CM position and solar pressure torque are added in chapter 6:

Case	$\omega_{1/2}$ De-tumble time	ω residual
Higher sphere SMSM, $\boldsymbol{b_1}$ deviation	220 [h]	[≈ 0, ≈ 0, 0.7] [deg/s]
Higher sphere SMSM, $\boldsymbol{b_3}$ deviation	240 [h]	[≈ 0, ≈ 0, 0.5] [deg/s]
Lower sphere SMSM, $\boldsymbol{b_1}$ deviation	270 [h]	[≈ 0, ≈ 0, 1.7] [deg/s]
Lower sphere SMSM, $\boldsymbol{b_3}$ deviation	280 [h]	[≈ 0, ≈ 0, 0.5] [deg/s]

Table 7.4: Robustness analysis for the box and panel service case

If the spheres model used is not precise enough, the axis- symmetric system is unstable to small deviations of the center of mass along non symmetry axes, so great care must be taken in selecting models with an appropriate sphere count. Moreover the less precise model also takes longer to bring the angular velocity components to zero. Deviations along the symmetry axis only increase the total de-tumbling time instead.
The introduction of an Active Disturbance Rejection Control improves both the robustness and performance considerably, granting a complete de-tumble for all analyzed cases with a precise enough model. In addition, for a lower sphere count model the unstable behavior is avoided if the uncertainty in the inertia components is less than 10%.

Case	$\omega_{1/2}$ De-tumble time	ω residual
Lower spheres, low dev., low ΔJ	500 [h]	[≈ 0, ≈ 0, ≈ 0] [deg/s]
Lower spheres, high dev., low ΔJ	360 [h]	[≈ 0, ≈ 0, ≈ 0] [deg/s]
Lower spheres, low dev., high ΔJ	580 [h]	[≈ 0, ≈ 0, 0.5] [deg/s]
Lower spheres, high dev., high ΔJ	550 [h]	[≈ 0, ≈ 0, >2] [deg/s]
Higher spheres, low dev., low ΔJ	480 [h]	[≈ 0, ≈ 0, ≈ 0] [deg/s]
Higher spheres, high dev., low ΔJ	420 [h]	[≈ 0, ≈ 0, ≈ 0] [deg/s]
Higher spheres, low dev., high ΔJ	600 [h]	[≈ 0, ≈ 0, ≈ 0] [deg/s]
Higher spheres, high dev., high ΔJ	550 [h]	[≈ 0, ≈ 0, ≈ 0] [deg/s]

Table 7.5: ADRC enhanced control cases with high and low deviation (7 cm - 14 cm) and inertia uncertainty (2.5% - 12.5%)

In all the cases analyzed higher deviations help the system to de-tumble faster, and higher ΔJ uncertainties increase the total de-tumbling time. This also confirms that an object less axis-symmetric is easier to de-tumble since higher torques can be generated.

7.2 Further steps and challenges

In future work more cases and different geometries should be analyzed, in order to gain a better understanding of how the geometry of the service spacecraft affects the control performance. Moreover the impact of the attitude of the service spacecraft on the control performance could be modeled too. It may be possible to optimize the de-tumbling control further by changing the attitude of the service spacecraft too, so a control law able to take advantage of this could grant smaller de-tumble times. Regardless of these improvements it's clear that this technology has proved very promising and a valid solution to help solve the debris accumulation issues in GEO. At this point more research needs to be done on different aspects that are more specific on the systems of the service spacecraft itself, like the ion gun control, remote sensing of the debris potential to ensure that the correct electric Voltage is imposed and much more.

Appendix A

Numerical simulation parameters

In this section the data used to obtain the results and plots present in the paper are given, in particular the parameters and dimensions of the objects examined, initial conditions considered, and the deviations and uncertainties randomly selected for testing the ADRC.
In all cases, unless stated otherwise, the initial angular velocities and initial quaternion vector are respectively $\boldsymbol{\omega}_{B0}$ = [-1.374;1.374;0.5] [deg/s] and $\boldsymbol{q}_0$ = [0;0;0;1]. The integration method used is ODE113 with relative and absolute tolerances of 10^{-9} and 10^{-8}.
Also when inertia matrix uncertainties are considered, the unknown real $[J]$ is obtained by adding a certain percentage of the mean inertia value of the ideal one, to all elements multiplied by a random number between 0 and 1.

Table A.1: Simulation data for cases with no uncertainties

(a) Data for sphere and cylinder debris case in Fig.5.2

Parameter	**Value**	**Description**
R_s	2 [m]	Spherical spacecraft radius
R_d	1 [m]	Cylinder radius
h	3 [m]	Cylinder height
I_1	125 [kg m^2]	Debris axial inertia
I_2, I_3	812.5 [kg m^2]	Debris transverse inertia
V_{max}	$\pm$20 [kV]	Maximum potential imposed
$R_1 - R_3$	0.5909 [m]	External spheres radius
R_2	0.6512 [m]	Middle sphere radius
l	1.1569 [m]	External spheres offset from center of cylinder
R_{deb}	1.7334 - 1.4313 [-]	α for debris spheres (56-112)
R_{serv}	1.9 - 1.9 [-]	α for service spheres (60-100)

(b) Data for cubic spacecraft and cylinder debris case in Fig.5.3

Parameter	**Value**	**Description**
L_c	1x1x1 [m]	Cubic spacecraft size
L_p	2x1 [m]	Solar panels size
R_d	1 [m]	Cylinder radius
h	3 [m]	Cylinder height
I_1	125 [kg m^2]	Debris axial inertia
I_2, I_3	812.5 [kg m^2]	Debris transverse inertia
V_{max}	$\pm$20 [kV]	Maximum potential imposed
R_{deb}	1.628 - 1.4313 [-]	α for debris spheres (84-112)
R_{serv}	1.3180 - 1.3420 [-]	α for service spheres (68-160)

Table A.2: Simulation data for cases with uncertainties

(a) Data for unstable cases in Fig.6.2 and Fig.6.3

Parameter	Value	Description
L_c	1x1x1 [m]	Cubic spacecraft size
L_p	2x1 [m]	Solar panels size
R_d	1 [m]	Cylinder radius
h	3 [m]	Cylinder height
I_1	125 [kg m^2]	Debris axial inertia
I_2, I_3	812.5 [kg m^2]	Debris transverse inertia
V_{max}	$\pm$20 [kV]	Maximum potential imposed
$\|\boldsymbol{\delta}_1\|$ $\|\boldsymbol{\delta}_2\|$	2 [cm]	CM deviation along transversal axis
$\|\boldsymbol{\delta}_3\|$	20 [cm]	CM deviation along symmetry axes

(b) Data for control shutoff and no inertia uncertainty case in Fig.6.6

Parameter	Value	Description
L_c	1x1x1 [m]	Cubic spacecraft size
L_p	2x1 [m]	Solar panels size
R_d	1 [m]	Cylinder radius
h	3 [m]	Cylinder height
I_1	125 [kg m^2]	Debris axial inertia
I_2, I_3	812.5 [kg m^2]	Debris transverse inertia
V_{max}	$\pm$20 [kV]	Maximum potential imposed
$\|\boldsymbol{\delta}_1\|, \|\boldsymbol{\delta}_2\|$	2 [cm]	CM deviation along transversal axis
$\|\boldsymbol{\delta}_3\|$	20 [cm]	CM deviation along symmetry axes
k	3 [-]	Shutoff condition

(c) Data for ADRC case in Fig.6.9 and Fig.6.10

Parameter	Value	Description
L_c	1x1x1 [m]	Cubic spacecraft size
L_p	2x1 [m]	Solar panels size
R_d	1 [m]	Cylinder radius
h	3 [m]	Cylinder height
I_1	125 [kg m^2]	Debris axial inertia
I_2, I_3	812.5 [kg m^2]	Debris transverse inertia
V_{max}	$\pm$20 [kV]	Maximum potential imposed
$\boldsymbol{\delta}$	[4, -2.5, 6] and [8, -5, 12] [cm]	CM deviations considered
$[\Delta J_1]$ percentage	5% - 10% -12.5%	Inertia Uncertainty for Fig.6.9
$[\Delta J_2]$ percentage	2.5% - 5% -10%	Inertia Uncertainty for Fig.6.10
β_1, β_2	0.5 - 50 [-]	Full state observer gains

Bibliography

[1] D. L. Oltrogge, S. Alfano, C. Law, A. Cacioni, and T. S. Kelso. "A comprehensive assessment of collision likelihood in Geosynchronous Earth Orbit". In: *Acta Astronautica* 147 (2018), pp. 316, 345. DOI: 10.1016/j.actaastro.2018.03.017.

[2] R. Jehn and C.Hernandez. "International practices to protect the geostationary ring". In: *Space Debris* 1 (2001), pp. 221, 233. DOI: 10.1016/j.actaastro.2013.08.023.

[3] R. Jehn, V. Agapov, and C. Hernandez. "The situation in the geostationary ring". In: *Advances in Space Research* 35.7 (2005), pp. 1318, 1327. DOI: 10.1016/j.asr.2005.03.022.

[4] P. V. Anderson and H. Schaub. "Local debris congestion in the geosynchronous environment with population augmentation". In: *Acta Astronautica* 94.2 (2014), pp. 619, 628. DOI: 10.1016/j.actaastro.2013.08.023.

[5] N. Johnson. "Protecting the geo environment: policies and practices". In: *Space Policy* 15.3 (1999), pp. 127, 135. DOI: 10.1016/S0265-9646(99)00022-3.

[6] P. Chrystal, D. McKnight, P. L. Meredith, J. Schmidt, M. Fok, and C. Wetton. "Space debris: On collision course for insurers". In: *Swiss Reinsurance Company Ltd Tech report* (March 2011).

[7] A. Caubet and J.D. Biggs. "Design of an attitude stabilization electromagnetic module for detumbling uncooperative targets". In: *IEEE Aerospace Conference*. 2014.

[8] P. Couzin, F. Teti, and R. Rembala. "Active removal of large debris : Rendez-vous and robotic capture issues". In: *2nd European Workshop on Active Debris Removal*. Paris, France, 2012.

[9] Couzin, P., Teti F., and Rembala R. "Active removal of large debris: system approach of deorbiting concepts and technological issues". In: *6th European Conference on Space Debris*. Darmstadt, Germany, 2013.

[10] Kaplan and M. H. "Dynamics and control of detumbling a disabled spacecraft during rescue operations". In: *NASA technical report* NASA-CR-135788, AAR-73-10 (1973).

[11] R. A. Gangapersaud, G. Liu, and A. H.J.de Ruiter. "Detumbling a Non-cooperative Target with Unknown Inertial Parameters using a Space Robot Under Control Input Magnitude Constraint". In: *Advances in Space Research* 63.12 (2019), pp. 3900, 3915.

[12] Yu S. Karavaev, R. M Kopyatkevich, M. N. Mishina, G. S. Mishin, P. G. Papushev, and P. N. Shaburov. "The dynamic properties of rotation and optical characteristics of space debris at geostationary orbit". In: *Advances in the Astronautical Sciences* 119.AAS-04-192 (2004), pp. 1457, 1466.

[13] Yu S. Karavaev, M. N. Mishina, and P. G. Papushev. "Investigations of the evolution of optical characteristics and dynamics of proper rotation of uncontrolled geostationary artificial satellites". In: *Advances in Space Research* 43.9 (2009), pp. 1416, 1422.

[14] D. McKnight, F. Pentino, A. Kaczmarek, and S. Knowles. "Detumbling rocket bodies in preparation of active debris removal". In: *6th European conference on space debris*. Darmstat, Germany, 2013.

[15] V. S. Aslanov and A. S. Ledkov. "Attitude Motion of Cylindrical Space Debris during Its Removal by Ion Beam". In: *Mathematical Problems in Engineering* (2017). DOI: 10.1155/2017/1986374.

[16] C. Bombardelli and J. Peláez. "Ion Beam Shepherd for Contactless Space Debris Removal". In: *American Institute of Aeronautics and Astronautics* (2010). DOI: 10.2514/1.51832.

[17] T. Bennett, D. Stevenson, E. Hogan, and H. Schaub. "Prospects and challenges of touchless electrostatic detumbling of small bodies". In: *Advances in Space Research* 56.3 (2015), pp. 557, 568. DOI: 10.1016/j.asr.2015.03.037.

[18] P. V.Anderson and H. Schaub. "Conjunction challenges of low-thrust geosynchronous debris removal maneuvers". In: *Acta Astronautica* 123 (2016), pp. 154, 164. DOI: 10.1016/j.actaastro.2016.03.014.

[19] H. Schaub and D. F. Moorer Jr. "Geosynchronous Large Debris Reorbiter: Challenges and Prospects". In: *The Journal of the Astronautical Sciences* 59.1 2 (2012), pp. 165, 180.

[20] H. Schaub and Z. Sternovsky. "Active space debris charging for contactless electrostatic disposal maneuvers". In: *Advances in Space Research* 53 (2014), pp. 110, 118.

[21] T. Bennett and H. Schaub. "Contactless electrostatic detumbling of axi-symmetric GEO objects with nominal pushing or pulling". In: *Advances in Space Research* 62.11 (2018), pp. 2977, 2987. DOI: 10.1016/j.asr.2018.07.021.

[22] V. Aslanov and H. Schaub. "Detumbling Attitude Control Analysis Considering an Electrostatic Pusher Configuration". In: *Journal of guidance, control and dynamics* 42.4 (2019). DOI: 10.2514/1.G003966.

[23] A.C. Tribble. "The Space Environment, Implications for Spacecraft Design," in: *revised and expanded ed Princeton University Press* (2003).

[24] Dento, M.H., Thomsen, M.F., Korth, H., Lynch, Zhang, J.C.and Liemohn, and M.W. "Bulk plasma properties at geosynchronous orbit". In: *Journal of Geophysical Research, A7, 110* (2005).

[25] C.R. Seubert, L. A. Stiles, and H. Schaub. "Effective Coulomb force modeling for spacecraft in Earth orbit plasmas". In: *American Institute of Aeronautics and Astronautics* (2010). DOI: 10.2514/1.51832.

[26] T. Bennett and H. Schaub. "Touchless Electrostatic Three-dimensional Detumbling of Large Axi-symmetric Debris". In: *The Journal of the Astronautical Sciences* 62 (2015), pp. 233, 254. DOI: 10.1007/s40295-015-0075-8.

[27] D. Stevenson and H. Schaub. "Multi-Sphere Method for modeling spacecraft electrostatic forces and torques". In: *Advances in Space Research* 51.1 (2013), pp. 10, 20. DOI: 10.1016/j.asr.2012.08.014.

[28] J. A. Hughes and H. Schaub. "Heterogeneous Surface Multisphere Models Using Method of Moments Foundations". In: *Journal of spacecraft and rockets* 56.4 (2019). DOI: 10.2514/1.A34434.

[29] Y. Bai, J.D. Biggs, F. Bernelli Zazzera, and N. Cui. "Adaptive Attitude Tracking with Active Uncertainty Rejection". In: *Journal of Guidance Control and Dynamics* 41.2 (2018), pp. 546, 554. DOI: 10.2514/1.G002391.

[30] J. Han. "From PID to Active Disturbance Rejection Control". In: *IEEE TRANSACTIONS ON INDUSTRIAL ELECTRONICS* 56.3 (2009). DOI: 10.1109/TIE.2008.2011621.

[31] Y. Bai, J.D. Biggs, X. Wang, and N. Cui. "A singular adaptive attitude control with active disturbance rejection". In: *European Journal of Control* 35 (2017), pp. 50, 56. DOI: 10.1016/j.ejcon.2017.01.002.

[32] Yi Huang and W. Xue. "Active disturbance rejection control: Methodology and theoretical analysis". In: *ISA Transactions* 53 (2014), pp. 963, 976. DOI: 10.1016/j.isatra.2014.03.003.

[33] D. Stevenson and H. Schaub. "Optimization of Sphere Population for Electrostatic Multi-Sphere Method". In: *IEEE Transactions on plasma science* 41.12 (2013), pp. 3526, 3535. DOI: 10.1109/TPS.2013.2283716.

[34] J. Maxwell, K. T. H. Wilson, M. Ghanei, and H. Schaub. "Multi-Sphere Method For Flexible Conducting Space Objects: Modeling And Experiments". In: *AAS/AIAA Astrodynamics Specialist Conference*. AAS 18-400. Snowbird, UT, 2018.

[35] P. Chow, J. Hughes, T. Bennett, and H. Schaub. "Automated Sphere Geometry Optimization For The Volume Multi Sphere Method". In: *26th AAS/AIAA Spaceflight Mechanics Meeting, Napa Valley, California* (2016).

[36] G. Ingram, J. Hughes, T. Bennett, C. Reilly, and H. Schaub. "Volume Multi-Sphere-Model Development Using Electric Field Matching". In: *The Journal of the Astronautical Sciences* 65 (2018), pp. 377, 399. DOI: 10.1007/s40295-018-0136-x.

[37] Microsoft. *3D Builder*. 2013. URL: https://www.microsoft.com/it-it/p/3d-builder/9wzdncrfj3t6?activetab=pivot:overviewtab.

[38] P. Cignoni, M. Callieri, M. Corsini, M. Dellepiane, F. Ganovelli, and G. Ranzuglia. *MeshLab: an Open-Source Mesh Processing Tool*. 2008. URL: http://www.meshlab.net/.

[39] J. Maxwell and H. Schaub. "Applicability Of The Multi-Sphere Method To Flexible One-Dimensional Conducting Structures". In: *AAS/AIAA Astrodynamics Specialist Conference*. Paper No. AAS-17-618. Stevenson, WA, 2017.

[40] V. Pesce, M. Lavagna, and R. Bevilacqua. "Stereovision-based pose and inertia estimation of unknown and uncooperative space objects". In: *Advances in Space Research* 59 (2017), pp. 236, 251. DOI: 10.1016/j.asr.2016.10.002.

[41] E. Tweddle, A. Saenz-Otero, J. Leonard, and D. W. Miller. "Factor Graph Modeling of Rigid-body Dynamics for Localization, Mapping, and Parameter Estimation of a Spinning Object in Space". In: *Journal of field robotics* 32.6 (2018), pp. 805, 817. DOI: 10.1002/rob.21548.

[42] R. Volpe, G. B. Palmerini, and M. Sabatini. "A passive camera based determination of a non-cooperative and unknown satellite's pose and shape". In: *Acta astronautica* 151 (2015), pp. 233, 254. DOI: 10.1016/j.actaastro.2018.06.061.

[43] H. Schaub. *Analytical Mechanics of Space Systems, Fourth Edition*. 2018.

[44] T. Bennett and H. Schaub. "Capitalizing on realtive motion in electrostatic detumbling of axi-symmetric GEO objects". In: *6th International Conference on Astrodynamics Tools and Techniques (ICATT)*. Darmstat, Germany, 2016.

[45] J. A. Hughes and H. Schaub. “Spacecraft Electrostatic Force and Torque Expansions Yielding Appropriate Fidelity Measures”. In: *The Journal of astronautical sciences* 66 (2019), pp. 46, 67. DOI: 10.1007/s40295-019-00154-7.